*machines*

MDPI

*Article*

# Reshaping Load-Dependent Mesh Excitation Waveforms of Spur Gears—An Analytical Framework on Tip Relief Modeling and Design

**Xingyuan Zheng [1,2,*], Weidong Zhu [3], Gang Li [4] and Yumei Hu [1]**

[1] College of Mechanical and Vehicle Engineering, Chongqing University, Chongqing 400044, China; cdrhym@cqu.edu.cn
[2] Department of Mechanical Engineering, University of Utah, Salt Lake City, UT 84112, USA
[3] Department of Mechanical Engineering, University of Maryland Baltimore County, Baltimore, MD 21250, USA; wzhu@umbc.edu
[4] Michael W. Hall School of Mechanical Engineering, Mississippi State University, Starkville, MS 39762, USA; gli@me.msstate.edu
* Correspondence: zhengxingyuan@cqu.edu.cn or xingyuan.zheng@utah.edu

**Abstract:** Tip relief is a critical design feature of modern spur gears, aimed at improving dynamic performance through a typical design strategy involving peak-to-peak minimization of mesh excitations. However, due to the hyperstatic nature of simultaneous tooth engagements, the applied torque not only affects mesh deformation amplitudes as normally considered but also alters mesh excitation waveforms, leaving great challenges for the typical design to meet various operating conditions. This paper develops an analytical framework to reshape mesh excitation waveforms, aimed at flexibly reducing vibration intensities across different operating loads and speeds. The load-dependency of excitation harmonics with tip relief is efficiently characterized by an improved analytical mesh excitation model. A tip relief design method is proposed, which automatically recombines harmonic contents of mesh excitations to adapt target operating speeds. Comparisons with finite element models and experiments confirmed the accuracies of quasi-static and dynamic analyses. Parametric studies and application examples further demonstrate the acceptable feasibility and effectiveness of the present method.

**Keywords:** spur gears; mesh excitations; analytical modeling; nonlinear dynamics; tip relief design

check for updates

Academic Editor: Ciro Santus

Received: 19 January 2025
Revised: 16 February 2025
Accepted: 17 February 2025
Published: 18 February 2025

**Citation:** Zheng, X.; Zhu, W.; Li, G.; Hu, Y. Reshaping Load-Dependent Mesh Excitation Waveforms of Spur Gears—An Analytical Framework on Tip Relief Modeling and Design. *Machines* **2025**, *13*, 161. https://doi.org/10.3390/machines13020161

**Copyright:** © 2025 by the authors. Licensee MDPI, Basel, Switzerland. This article is an open access article distributed under the terms and conditions of the Creative Commons Attribution (CC BY) license (https://creativecommons.org/licenses/by/4.0/).

## 1. Introduction

Growing demands for high-power density transmissions enforce modern spur gears to be lightweight under heavy-load conditions. Flexible control of vibration intensities under different operating conditions is becoming increasingly important [1–4]. Both profile modifications (e.g., tip and root relief, profile slope, profile crowning) and flank modifications (e.g., end relief, lead slope, lead crowning), are important techniques used to improve mesh performances. Differing from evening contact loads and reducing stress concentrations by flank modifications, profile modifications completely alter the involute profile of the gear tooth in the direction of motion, which directly influences mesh excitation sources and vibration responses. Compared with root relief, tip relief can effectively reduce vibrations by suitably trimming tip profiles without reducing root strength, becoming a critical design feature of modern spur gears. In a geometric sense, the micron-sized material removal by tip relief is negligible compared with the macro gear structure. However, this slight shift in

the tip profile completely alters tooth contact regions and deformation compatibilities [5–7], inducing noticeable changes in mesh performance [8]. Reliable tip relief design depends on accurate modeling of the underlying mesh mechanisms [9].

One unique nature of spur gear transmission lies in alternating tooth engagements, where multi-harmonic and time-varying mesh excitations characterize dynamic behaviors and guide parameter designs. For gear transmissions, mesh stiffness and loaded static transmission error (LSTE) are primary sources of mesh excitations [10]. Mesh stiffness represents the gear mesh deformability, which inevitably fluctuates with time-varying mesh positions. LSTE comprehensively covers elastic deformations and displacement errors during gear mesh, defined as the deviation between a pair of gears along the line of action (LOA) in quasi-static loading conditions. As key indexes for gear analyses and designs, mesh stiffness, and LSTE have attracted paramount concerns in recent decades [11–13].

Due to the accuracy in deformation computation, finite element models (FEMs) with both bi-dimensional [14–18] and three-dimensional elements [19–21] have been widely adopted to evaluate mesh stiffness and LSTE [11]. To reduce computation expenses, some researchers further developed finite element/contact mechanics models [22–24] and hybrid FEM-analytical models [25–28]. However, FEM-based simulations are time-consuming due to the large number of discrete elements, especially for extensive parametric studies in the initial design stages [29].

Compared to FEMs, analytical models are more flexible and efficient for deep insights into mesh mechanisms [12]. Pioneer studies found a typical framework to evaluate mesh stiffness and LSTE, where the complex gear structure is divided into relatively simple substructures, including the gear tooth and the fillet foundation. The mesh deflection then follows the superposition along LOA. The gear tooth is normally idealized as a taper cantilever beam to embody the combined effects of axial compression, bending, shearing, and Hertzian contact [30–32]. The fillet foundation occupies the main gear structure and largely influences the mesh deflection. Sainsot [33] derived a fillet foundation stiffness induced by the local mesh force and curve-fitted the plane strain solutions with polynomials. Later, Xie [34] extended the plane strain polynomials to cover the structural coupling of the fillet foundation in double tooth contact. With analytical models, profile modifications are extensively studied on the aspects of mesh performance [35–38], dynamics [39–43], lubrication [44–47], tooth stresses [48–50], and tooth failures [36,51,52].

The above works laid the foundations for tip relief design. Generally, the primary target of tip relief design involves smoothing fluctuations of mesh excitations by choosing suitable modification lengths, amounts, and shapes. Minimizing the peak-to-peak value of LSTE is the most common optimization objective [13]. However, as indicated by relevant studies [53,54], minimizing the overall variation can improve dynamic performance, specifically within speed intervals nearing the primary in-phase mode [54], but it may conversely increase dynamic response for other speed intervals in geared systems [53]. More flexible and pertinent strategies are required if these intervals are rated speed conditions.

Waveforms of mesh stiffness and LSTE are commonly described with the theoretical mesh intervals in most analytical models. However, during gear mesh, a phenomenon called extended tooth contact (ETC) would arise, i.e., under the applied torque, the deformation of fillet foundation inevitably brings transport motions to the surrounding teeth, trending the theoretically separated teeth to engage. The shifted mesh intervals further change the waveforms of mesh stiffness and LSTE, causing harmonic contents to become load-dependent. Moreover, tooth deviations introduced by tip relief would be involved in the extended tooth contact and further complicate the tip relief design. This phenomenon attracted increasing attention in recent studies [55–58] where polynomial formulas [33,34] are used as fundamental theories. Whereas, due to inherent limitations of curve-fitting in

plane strain, restrictions still exist in these formulas, such as the case of plane stress for thin-walled gears and the confidence intervals. Recently, Zheng et al. [59,60] developed an analytical mesh stiffness model to remove such restrictions of polynomial formulas. Unfortunately, in-depth studies on the tip relief modeling and design remain uncovered.

This paper presents an analytical framework of tip relief modeling and design, aiming to provide a flexible strategy to reshape mesh excitations and control vibrations. An improved analytical mesh excitation model is proposed to characterize the load dependency of excitation harmonics with tip relief, which ensures adaptability for various spur gear typologies and applied torques. Unlike typical design strategies, a double-searching method for tip relief design is proposed to automatically recombine harmonic contents of mesh excitations, further ensuring flexible control of vibrations near target speed intervals. The accuracies of quasi-static and dynamic analyses are verified by FEMs and experiments. Parametric studies and application examples further confirm the feasibility and effectiveness of the present framework.

The rest of this paper is organized as follows: Section 2 introduces basic considerations of the proposed analytical framework; Sections 3 and 4 detail the proposed analytical framework. The results and discussions are further presented in Sections 5 and 6. Some algebras, parameters, FEMs, and nomenclature are summarized in the appendices.

## 2. Basic Considerations

Figure 1 summarizes the difference between general and current considerations on tip relief modeling and design. Gear vibrations are closely related to the transmission error (TE). By definition, the transmission error measures the departure from the perfectly conjugate gear motion transfer between tooth pairs [61]. Ideally, for non-deformable gear teeth with perfect tooth profiles and installations, the TE vanishes. However, due to interactions between mesh-in/out, mesh deformations, and tooth deviations of practical tooth pairs under applied torque, the TE fluctuates during meshing, resulting in complex mesh excitations (Figure 1a,b).

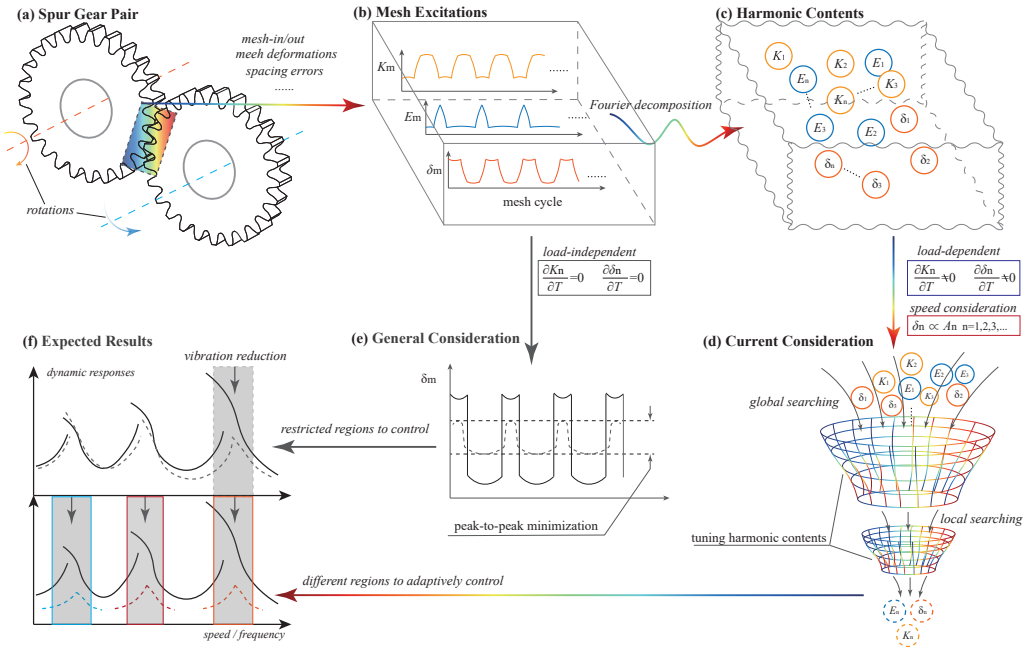


**Figure 1.** A sketch of general and current considerations on tip relief design.

In the quasi-static loading state, the transmission error (TE) is also called the loaded static transmission error (LSTE) [8,26]. Under this circumstance, both mesh deformations

under applied torque and geometrical deviations would contribute to the total quasi-static transmission error [23], leading to the following:

$$\delta_{\mathrm{m}} = \frac{T}{R_{\mathrm{b,p}} K_{\mathrm{m}}} + E_{\mathrm{m}},\ E_{\mathrm{m}} = E_{\mathrm{m,D}} + E_{\mathrm{m,M}}, \tag{1}$$

where $\delta_{\mathrm{m}}$ is the LSTE; the term $T/(R_{\mathrm{b,p}} K_{\mathrm{m}})$ represents mesh deflections of tooth pairs along the line of action in quasi-static loading; $K_{\mathrm{m}}$ denotes mesh stiffness; $T$ is the applied torque; $R_{\mathrm{b,p}}$ is the base circle radius of the pinion (the driving side with applied torque); the term $E_{\mathrm{m}}$ represents geometric deviations, commonly denoted as non-loaded static transmission errors (NSTEs) [8]. Typically, the NSTE is a superposition of geometric deviations ($E_{\mathrm{m,D}}$) caused by tooth modifications in design (e.g., tip relief and root relief) and geometric deviations ($E_{\mathrm{m,M}}$) caused by manufacturing imperfections (e.g., pitch, tooth profile deviations, run-out tolerances). At the current stage, by omitting the term $E_{\mathrm{m,D}}$, we emphasize reflecting independent correlations between tip relief parameters and mesh mechanisms in the initial design. Thus, tip relief design can be treated as adjusting the mesh excitations by introducing intentional tooth deviations. NSTE and LSTE can be described in the forms of angular rotational differences [62,63] or the differences along the line of action [23,64,65]. To facilitate the subsequent modelings, this paper describes NSTE and LSTE in the latter way.

For various engineering requirements, tip relief design should provide reliable vibration reductions at specified working conditions. In general considerations, the common strategy involves choosing tip relief configurations that minimize the peak-to-peak value of the LSTE curve (Figure 1e). However, due to oversimplified considerations in tip relief modeling and design, the conventional strategy may lack the robustness needed to meet different working conditions, particularly the following:

- **Tip relief modeling:** Mesh excitations are typically estimated in mesh intervals with boundaries defined by the theoretical HPSTC/LPSTC (highest/lowest point of single-tooth contact). However, due to the extended tooth contact, the actual mesh interval is load-dependent [59]. For a more reliable tip relief design to meet different applied torques, load dependencies of mesh excitations should be fully captured.
- **Tip relief design**: Minimizing the peak-to-peak value of the LSTE curve may effectively reduce the overall vibration amplitude. However, higher orders of harmonic contents cannot be flexibly controlled, restricting the speed/frequency interval for robust vibration reduction near the primary resonance (Figure 1f). If the specified speed/frequency is beyond this interval, the conventional design method should be reconsidered.

Unlike the typical approach of directly adjusting the LSTE curve, the current work delves deeper into tuning the harmonic contents of mesh excitations (Figure 1c,d), which is expected to flexibly reduce vibration intensities at different applied torques and operating speeds (Figure 1f). The modeling and design strategy stems from considerations of the applied torque and operating speed in the mesh mechanism, as detailed in Sections 2.1 and 2.2.

### *2.1. Considerations on the Applied Torque*

The fillet foundation deformed by the applied torque brings transport motions to the surrounding teeth [34,59], forcing theoretically separated tooth pairs to engage. This load-dependent phenomenon is typically called extended tooth contact (ETC). The designed tip relief, in the case of ignoring ETC (Figure 2a), may have delayed the engagement of tooth pair 1. However, due to the ETC effect, deformations of the fillet foundation would force the modified tooth pair 1 to engage (Figure 2b), indicating that the trimming of the tip

profile is insufficient. In addition, modern gears tend to be thin-walled for light-weighting (Figure 2c), increasing the sensitivity of the ETC effect to the applied torque.

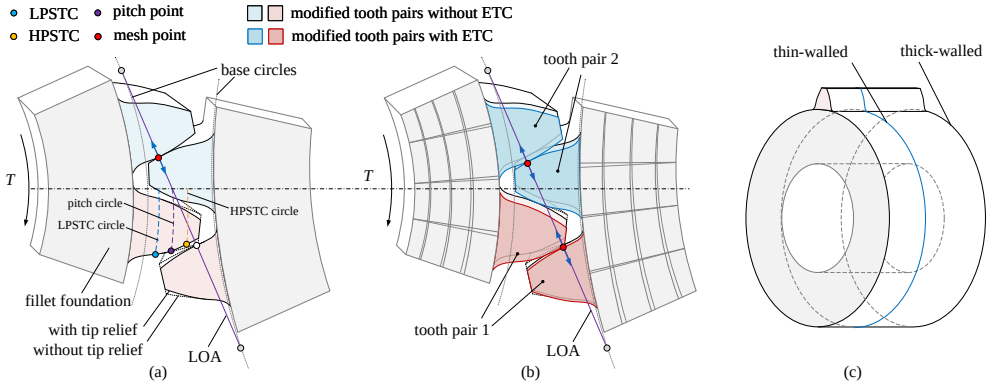


**Figure 2.** Conceptual difference between ignoring and considering the ETC of the modified gear pair: (**a**) tip relief in the scenario of ignoring ETC; (**b**) tip relief in the scenario of considering ETC; (**c**) thin-walled and thick-walled gear structures.

From the above descriptions, it can be concluded that the ETC effect and tip relief jointly influence mesh intervals, causing mesh excitations to become compound functions of the applied torque and tip relief configuration:

$$E_{\mathrm{m}} = E_{\mathrm{m}}(t, \wp),\ K_{\mathrm{m}} = K_{\mathrm{m}}(t, T, \wp),\ \delta_{\mathrm{m}} = \delta_{\mathrm{m}}(t, T, \wp), \tag{2}$$

where $t$ denotes time; and $\wp$ denotes tip relief configuration (detailed in Section 3.1). Periodic tooth engagements induce the multi-harmonic nature of mesh excitations. Inspired by Ref. [61], different mesh excitation waveforms are separately considered, and the Fourier series of mesh excitations can be written as follows:

$$E_{\mathrm{m}}(t, \wp) \approx E_0(\wp) + \sum_{n=1}^{N} E_n(\wp) \cos(2\pi n f_{\mathrm{m}} t - \phi_{E,n}), \tag{3}$$

$$K_{\mathrm{m}}(t, T, \wp) \approx K_0(T, \wp) + \sum_{n=1}^{N} K_n(T, \wp) \cos(2\pi n f_{\mathrm{m}} t - \phi_{K,n}), \tag{4}$$

$$\delta_{\mathrm{m}}(t, T, \wp) \approx \delta_0(T, \wp) + \sum_{n=1}^{N} \delta_n(T, \wp) \cos(2\pi n f_{\mathrm{m}} t - \phi_{\delta,n}), \tag{5}$$

where $E_0$, $K_0$, and $\delta_0$ are average values of $E_{\mathrm{m}}$, $K_{\mathrm{m}}$, and $\delta_{\mathrm{m}}$, respectively; $E_n$, $K_n$, and $\delta_n$ are the corresponding $n^{th}$ harmonic contents; $\phi_{E,n}$, $\phi_{K,n}$, and $\phi_{\delta,n}$ are phase angles; $f_{\mathrm{m}}$ is the mesh frequency. Throughout this paper, we let $N = 4$ for approximation.

It should be noted that the applied torque not only affects mesh deformation amplitudes as normally considered but also alters mesh intervals, resulting in load dependencies of harmonic contents $K_n = K_n(T, \wp)$, $\delta_n = \delta_n(T, \wp)$, which should be captured for adaptive tip relief design at different applied torques.

### *2.2. Considerations on the Operating Speed*

The load-dependent excitation waveforms further influence the dynamic responses, where the dynamic transmission error (DTE) is a key indicator. Essentially, DTE is a dynamic representation of LSTE, embodying system inertia. In a steady state, the Fourier series of DTE can be expressed as follows:

$$q_{\mathrm{m}}(t, T, \wp) = A_0(T, \wp) + \sum_{n=1}^{\infty} A_n(T, \wp) \cos(2\pi n f_{\mathrm{m}} t - \phi_{q,n}), \tag{6}$$

where $q_{\mathrm{m}}$ is the DTE; $\phi_{q,n}$ are the phase angles of DTE. $A_0$ and $A_n$ denote the average value and harmonic contents of DTE. From the phenomenology that both LSTE and DTE signify the rotational deviation of the gear pair, a reasonable presupposition can be inferred as follows:

$$\delta_n(T, \wp) \propto A_n(T, \wp),\ n = 1, 2, 3, \ldots, \tag{7}$$

such a harmonic correlation is seldom discussed, and prior studies mainly focus on peak-to-peak values between LSTE and DTE for tip relief design. Equation (7) provides a clue to control $A_n$ by reshaping $\delta_n$, and the validity of Equation (7) is discussed in Section 6.1. Over a wide range of swept frequencies, multi-harmonic peaks formed by $A_n$ occur in the spectrum (e.g., primarily and super-harmonic resonances).

According to the experimental observations [64], each order of $A_n$ dominates the corresponding harmonic resonances, where the vibration amplitude peaks at $f_{\mathrm{n}}, f_{\mathrm{n}}/2, f_{\mathrm{n}}/3, \ldots$ for multi-harmonic resonances ($f_{\mathrm{n}}$-the natural frequency). Therefore, the problem of reducing the vibration intensity at a target speed or mesh frequency can be converted as follows: find the harmonic resonance frequencies near the target operating speed/frequency, and adjust excitation components $\delta_n$ to reduce the vibration components $A_n$.

Based on the above considerations, an analytical framework of tip relief modeling and design is further detailed in Sections 3 and 5.

## 3. A Tip Relief Design Method

In this section, a tip relief design method is proposed to control vibrations under different working conditions. For clarity, tip relief configuration is defined in Section 3.1. A double-searching process to flexibly select proper tip relief configurations is proposed in Section 3.2; Equations of motion with tip relief are further introduced in Section 3.3.

### *3.1. Definition of Tip Relief Configuration*

Tip relief is configured by the modification length, the modification amount, and the modification shape. In Figure 3a, the material removal starts from point $B$ and gradually increases with the angular position $\tau$ until reaching the tooth tip $A$. Here, $\tau_A$ and $\tau_B$ are angular positions of $A$ and $B$; and $C_{\mathrm{T}}$ and $L_{\mathrm{T}}$ are the modification amount and length at the tip circle, respectively. Based on the involute geometry, relations between $L_{\mathrm{T}}$, $\tau_A$, and $\tau_B$ are given by the following:

$$\tau_A = \alpha_a - \theta_b + \mathrm{inv}(\alpha_a),\ L_{\mathrm{T}} = R_a \cos(\alpha_a - \tau_A) - R_b[\cos\tau_B + (\tau_B + \theta_b)\sin\tau_B], \tag{8}$$

where $R_a$ is the tip circle radius; $\alpha_a = \arccos(R_b/R_a)$ is the pressure angle at the tip circle; $\theta_b$ is the half-tooth angle at the base circle; $\mathrm{inv}(\bullet)$ is the involute function. The modification amount of a generic point at the tooth flank, $f_{\mathrm{T}}$, is expressed as follows [56]:

$$f_{\mathrm{T}}(\tau, \wp) = \begin{cases} C_{\mathrm{T}}\left(\dfrac{\tau - \tau_B}{\tau_A - \tau_B}\right)^S, & \tau \in [\tau_B, \tau_A] \\ 0, & \tau \notin [\tau_B, \tau_A] \end{cases}, \tag{9}$$

where $S \in [1, 2]$ is a power exponent used to describe the shapes of modified tooth profiles. In particular, $S = 1, 2$, respectively, represent linear and parabolic modifications (Figure 3b).

The non-dimensional array $\wp$ describes the tip relief configuration:

$$\wp = \left\{\frac{L_{\mathrm{T}}}{L_{\mathrm{T,max}}}, \frac{C_{\mathrm{T}}}{C_{\mathrm{T,max}}}, S\right\} = \{L_{\mathrm{n}}, C_{\mathrm{n}}, S\}, \tag{10}$$

where $C_{T,max} = 0.02m$ and $L_{T,max} = 0.6m$ ($m$-the module) are the maximum values of $L_T$ and $C_T$ suggested by British Standard (BS 1970) and ISO (ISO/DIS 1983) [66,67]. $L_n$ and $C_n$ are normalized values of $L_T$ and $C_T$, respectively. For the unmodified case, $\wp$ is given by $\wp = \mathbf{0}$.

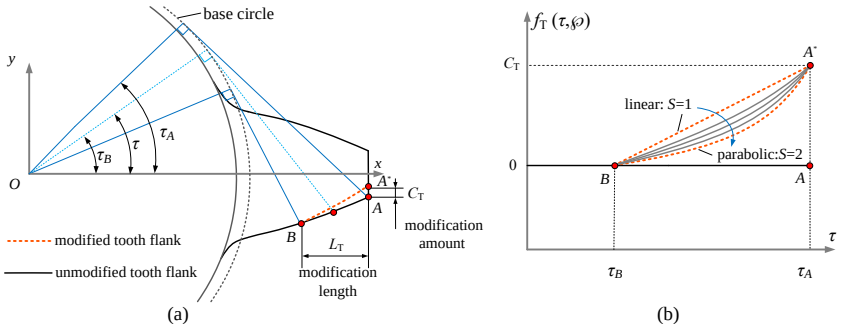


**Figure 3.** Schematic of tip relief: (**a**) the tooth geometry with tip relief; (**b**) the function $f_T(\tau, \wp)$.

### *3.2. A Double-Searching Process of Tip Relief Configurations*

In this section, a double-searching process is proposed to select the proper tip relief configurations. Based on considerations in Section 2 and the mesh excitation model in Section 4.2, the proposed process successively searches harmonic contents with tip relief parameters to reshape mesh excitations and adapt to different working conditions. Basically, the proposed process includes global searching and local searching, where global searching focuses on initially excluding excessive tip relief modifications and local searching further finds satisfactory combinations of excitation contents to control multiple harmonic resonances. Explanations and steps of the double-searching process are introduced as follows.

Tip relief influences each harmonic content of LSTE. By introducing non-dimensional coefficients $\omega_n(\wp), n = 0, 1, 2, 3, \ldots$, the changed harmonic contents are as follows: $\delta_n(T, \wp) = \omega_n \delta_n(T, \mathbf{0})$. For the same initial mesh position, LSTE waveforms between modified and unmodified cases are related as follows:

$$\delta_m(t, T, \wp) \approx \omega_0(\wp)\delta_0(T, \mathbf{0}) + \sum_{n=1}^{N} \omega_n(\wp)\delta_n(T, \mathbf{0}) \cos(2\pi n f_m t - \phi_{\delta,n}). \tag{11}$$

Mathematically, infinite combinations of $\omega_n(\wp)$ co-exist to reshape $\delta_m(t, T, \mathbf{0})$. Based on set theory, the proposed double-searching process aims to control the harmonic contents of LSTE and implicitly determine suitable combinations of $\omega_n(\wp)$ for different working conditions.

Figure 4 outlines the whole procedure, comprising four steps: Step 1: **mapping**; Step 2: **computing**; Step 3: **global searching**; and Step 4: **local searching**. Detailed descriptions of each step are summarized as follows:

- Step 1: **mapping**. This step aims to initialize the tip relief configuration $\wp = \{L_n, C_n, S\}$. The parameter $S$ is user-defined (e.g., $S = 1$ for linear modification and $S = 2$ for parabolic modification). Given the upper bounds $L_{n,max}$ and $C_{n,max}$, we have the following:

$$L_n \in [0, L_{n,max}],\ C_n \in [0, C_{n,max}], \tag{12}$$

$L_n$ and $C_n$ can be further uniformly discretized into the following:

$$\begin{cases} L_n \in \{L_{n,k}\}_{k=1,2,3,\ldots,N_L} = \left\{ \dfrac{(k-1)L_{n,max}}{N_L - 1} \right\}_{k=1,2,3,\ldots,N_L} \\ C_n \in \{C_{n,s}\}_{s=1,2,3,\ldots,N_C} = \left\{ \dfrac{(s-1)C_{n,max}}{N_C - 1} \right\}_{s=1,2,3,\ldots,N_C} \end{cases}, \tag{13}$$

where $k, s$ are counting numbers; $L_{\mathrm{n},k}$ and $C_{\mathrm{n},s}$ are discretized data points of $L_{\mathrm{n}}$ and $C_{\mathrm{n}}$. $N_L, N_C$ are the numbers of discretized data points. Such initialization generates the map shown in Figure 4a, laying the foundation for the subsequent steps.

- Step 2: **computing**. This step further computes mesh excitations, including the NSTE, mesh stiffness, and LSTE. By inputting the applied torque $T$, configurations $\wp = \{L_{\mathrm{n},k}, C_{\mathrm{n},s}, S\}$ and gear pair parameters (geometrical and material quantities), $E_{\mathrm{m}}$, $K_{\mathrm{m}}$, and $\delta_{\mathrm{m}}$ can be rapidly calculated based on the analytical mesh excitation model (detailed in Section 4). Harmonic contents $E_n$, $K_n$, and $\delta_n$ can be further obtained by Equations (3)–(5). Since evaluations of $E_n$, $K_n$, and $\delta_n$ for each $(L_{\mathrm{n},k}, C_{\mathrm{n},s})$ are mutually independent, parallel computing can be applied to speed up the calculation procedure (see Figure 4b).
- Step 3: **global searching**. Excessive tip relief modifications introduce unnecessary displacement excitations and conversely intensify vibrations. To avoid such situations, a global searching process is performed, ensuring that the fluctuation amplitudes of LSTE after modification are smaller than before. The set of $(L_{\mathrm{n},k}, C_{\mathrm{n},s})$ satisfying the above condition is given as follows:

$$\mathbb{S}_G = \left\{ (L_{\mathrm{n},k}, C_{\mathrm{n},s}) | \mathcal{L}_G(T, \wp) > 1 \right\}, \tag{14}$$

where $\mathbb{S}_G$ is the satisfied set. The dimensionless quantity $\mathcal{L}_G$ is defined by the ratio of the RMS of $\delta_n$ between modified cases and the unmodified case:

$$\mathcal{L}_G(T, \wp) = \left( \sum_{n=1}^{N} \delta_n^2(T, \mathbf{0}) \right)^{\frac{1}{2}} \cdot \left( \sum_{n=1}^{N} \delta_n^2(T, \wp) \right)^{-\frac{1}{2}}, \tag{15}$$

$\mathcal{L}_G(T, \wp) > 1$ indicates the overall fluctuation of LSTE is reduced after tip relief, and vice versa.

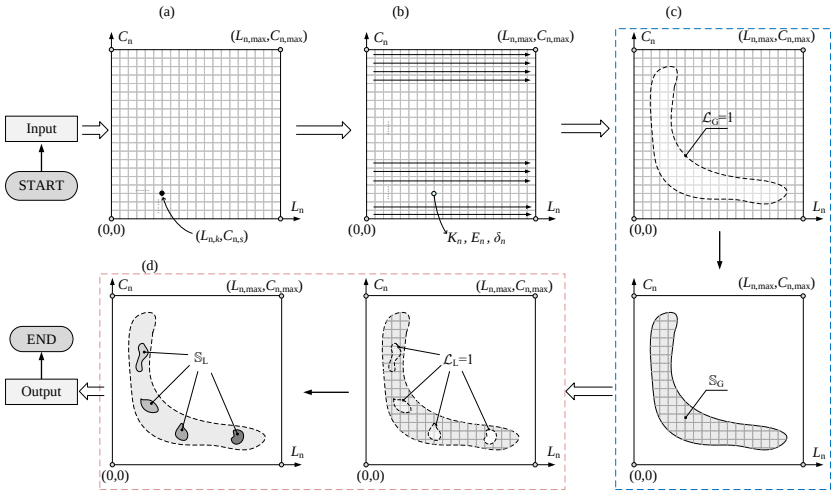


**Figure 4.** A double-searching process of tip relief parameters: (**a**) mapping; (**b**) computing; (**c**) global searching; (**d**) local searching.

Based on the $\delta_n$ at each coordinate $(L_{\mathrm{n},k}, C_{\mathrm{n},s})$ prepared in Step 2 and Equations (14) and (15), the searching gradually outlines the shape of $\mathbb{S}_G$ as illustrated in Figure 4c. Basically, the global search filters out most invalid tip relief parameters, leaving $\mathbb{S}_G$ as a "safe zone" for the subsequent local search.

- Step 4: **local searching**. The purpose of this step is to find satisfactory combinations of excitation contents to control multiple harmonic resonances (e.g., primary and super-harmonics). Within the previously obtained set $\mathbb{S}_G$, a local search process is further performed. A similar dimensionless quantity $\mathcal{L}_L$ is introduced as follows:

$$\mathcal{L}_L(T, \wp, \mathbf{W}) = \left( \sum_{n=1}^{N} W_n \delta_n^2(T, \mathbf{0}) \right)^{\frac{1}{2}} \cdot \left( \sum_{n=1}^{N} W_n \delta_n^2(T, \wp) \right)^{-\frac{1}{2}}, (L_{\mathrm{n},p}, C_{\mathrm{n},q}) \in \mathbb{S}_G, \quad (16)$$

where $\mathbf{W}$ is a vector of weight coefficients, satisfying the following:

$$\mathbf{W} = \{W_n\}_{n=1,2,3,\ldots,N}, \sum_{n=1}^{N} W_n = 1. \quad (17)$$

Evaluations of $\mathbf{W} = \{W_n\}_{n=1,2,3,4}$ are user-defined to reduce the emphasized resonance peaks. For example, to intentionally weaken the $n^{\mathrm{th}}, n = 1, 2, 3, 4$ harmonic resonance peaks, one has the following:

$$\begin{aligned} &\text{for } 1^{\mathrm{st}} \text{ harmonic} \rightarrow \mathbf{W} = \{1, 0, 0, 0\}, \text{ for } 2^{\mathrm{nd}} \text{ harmonic} \rightarrow \mathbf{W} = \{0, 1, 0, 0\}, \\ &\text{for } 3^{\mathrm{rd}} \text{ harmonic} \rightarrow \mathbf{W} = \{0, 0, 1, 0\}, \text{ for } 4^{\mathrm{th}} \text{ harmonic} \rightarrow \mathbf{W} = \{0, 0, 0, 1\}. \end{aligned} \quad (18)$$

The physical meaning of $\mathcal{L}_L$ refers to the reduction level of $\delta_n$ after tip relief. For more backup results, the maximum $H$ values of $\mathcal{L}_L$ (namely, $\mathcal{L}_{L,\max} = \mathcal{L}_{L,1} > \mathcal{L}_{L,2} > \mathcal{L}_{L,3} > \cdots > \mathcal{L}_{L,H}$) are selected as candidates. As illustrated in Figure 4d, the local search further outlines the corresponding intervals of $(L_{\mathrm{n},k}, C_{\mathrm{n},s})$, as follows:

$$\mathbb{S}_L = \left\{ (L_{\mathrm{n},k}, C_{\mathrm{n},s}) | \mathcal{L}_L(T, \wp, \mathbf{W}) \in \{\mathcal{L}_{L,1}, \mathcal{L}_{L,2}, \mathcal{L}_{L,3}, \ldots, \mathcal{L}_{L,H}\} \right\}. \quad (19)$$

Consequently, tip relief configurations within the set $\mathbb{S}_L$ can be regarded as desirable results, denoted by $\wp^* = (\mathbb{S}_L, S)$, which reshape waveforms of LSTE into the following:

$$\delta_{\mathrm{m}}(t, T, \wp^*) \approx \omega_0(\wp^*)\delta_0(T, \mathbf{0}) + \sum_{n=1}^{N} \omega_n(\wp^*)\delta_n(T, \mathbf{0}) \cos(2\pi n f_{\mathrm{m}} t - \phi_{\delta,n}), \quad (20)$$

where coefficients $\omega_n$ are automatically determined by $\omega_n = \delta_n(T, \wp^*)/\delta_n(T, \mathbf{0})$.

The above steps form a straightforward procedure for designing tip relief configurations. By implicitly determining suitable combinations of harmonic contents of LSTE, the specified vibration sources are controlled to adapt to different operating conditions.

### *3.3. Equations of Motion with Tip Relief*

For supporting elements (e.g., shaft and bearing) with relatively large rigidities, the vibration behavior of spur gear pairs can be effectively described using single-degree-of-freedom (SDOF) torsional vibration models [68]. In well-lubricated conditions, friction between tooth interfaces typically has secondary effects, and the equations of motion follow [68]:

$$J_{\mathrm{p}} \frac{d^2\theta_{\mathrm{p}}(t)}{dt^2} = T_{\mathrm{p}} - R_{b,\mathrm{p}} F_{\mathrm{m}}(t), \; J_{\mathrm{g}} \frac{d^2\theta_{\mathrm{g}}(t)}{dt^2} = R_{b,\mathrm{g}} F_{\mathrm{m}}(t) - T_{\mathrm{g}}, \quad (21)$$

where $\theta_{\mathrm{p}}$ and $\theta_{\mathrm{g}}$ are rotary displacements of pinion and gear, respectively; $J_{\mathrm{p,g}}$ and $T_{\mathrm{p,g}}$ refer to the corresponding rotary inertias and torques, respectively; $c_{\mathrm{m}}$ denotes the viscous damping of gear mesh; $b_{\mathrm{m}}$ is the half-backlash.

The dynamic mesh force $F_{\mathrm{m}}(t)$ is determined by the following:

$$F_{\mathrm{m}}(t) = K_{\mathrm{m}}(t, T, \wp) \cdot \mathcal{N}(q_{\mathrm{m}}(t), b_{\mathrm{m}}) + c_{\mathrm{m}} \left[ \frac{dq_{\mathrm{m}}(t)}{dt} - \frac{dE_{\mathrm{m}}(t, \wp)}{dt} \right], \quad (22)$$

where $q_{\mathrm{m}}(t) = \theta_{\mathrm{p}}(t)R_{b,\mathrm{p}} + \theta_{\mathrm{g}}(t)R_{b,\mathrm{g}}$ is the DTE. The piecewise function $\mathcal{N}(q_{\mathrm{m}}(t), b_{\mathrm{m}})$ condenses vibro-impact characteristics caused by backlash [1]:

$$\mathcal{N}(q_{\mathrm{m}}(t), b_{\mathrm{m}}) = \begin{cases} q_{\mathrm{m}}(t) - E_{\mathrm{m}}(t, \wp) - b_{\mathrm{m}} & q_{\mathrm{m}}(t) > b_{\mathrm{m}} \\ 0 & \mid q_{\mathrm{m}}(t) \mid \leq b_{\mathrm{m}} \\ q_{\mathrm{m}}(t) - E_{\mathrm{m}}(t, \wp) + b_{\mathrm{m}} & q_{\mathrm{m}}(t) < -b_{\mathrm{m}} \end{cases}. \tag{23}$$

Equation (21) can be reduced to a single equation in terms of $q_{\mathrm{m}}(t)$:

$$m_e \frac{\mathrm{d}^2 q_{\mathrm{m}}(t)}{dt^2} + c_{\mathrm{m}} \frac{dq_{\mathrm{m}}(t)}{dt} + K_{\mathrm{m}}(t, T, \wp) \cdot \mathcal{N}(q_{\mathrm{m}}(t), b_{\mathrm{m}}) = \frac{T}{R_{b,\mathrm{p}}} + \frac{d^2 E_{\mathrm{m}}(t, \wp)}{dt^2}, \tag{24}$$

where $m_e = J_{\mathrm{p}} J_{\mathrm{g}} / (J_{\mathrm{g}} R_{b,\mathrm{p}}^2 + J_{\mathrm{p}} R_{b,\mathrm{g}}^2)$ denotes the equivalent mass of the system. The nonlinear equation Equation (24) is numerically integrated by the 4th–5th-order Runge–Kutta method (RK45). The steady torque is applied to the pinion $T_{\mathrm{p}} = T$. The viscous damping $c_{\mathrm{m}}$ is determined by the damping ratio $\zeta$ and the average mesh stiffness $K_0(T, \wp)$, namely $c_{\mathrm{m}} = 2\zeta\sqrt{m_e K_0(T, \wp)}$. To capture bifurcations of gear dynamic response, time-stepping simulations, including the stepping-up/-down process, are adopted during frequency sweeping (see [18] for details).

## 4. An Analytical Mesh Excitation Model

### *4.1. Evaluation of NSTE*

Due to tip relief, material removals of tooth flanks introduce tooth deviations and further cause rigid body motions during mesh. The so-called NSTE refers to the resulting spacing errors due to geometric deviations.

To facilitate later discussions, spur gear pair configuration is pre-defined in Figure 5, where the driving side with the applied torque $T$ is defined as the pinion, and the driven side is named the gear. $F_i$ is the mesh force of tooth pair $i$ with action angle $\alpha_{Fi,j}$. Subscript $i = 1, 2$ represents quantities of tooth pair 1 and 2, respectively. Subscript $j$ is introduced to identify quantities of pinion ($j = \mathrm{p}$) and gear ($j = \mathrm{g}$). The force action angle of pinion tooth 1 is selected as a reference position angle of the system, namely, $\alpha_{F1,\mathrm{p}} = \tau$.

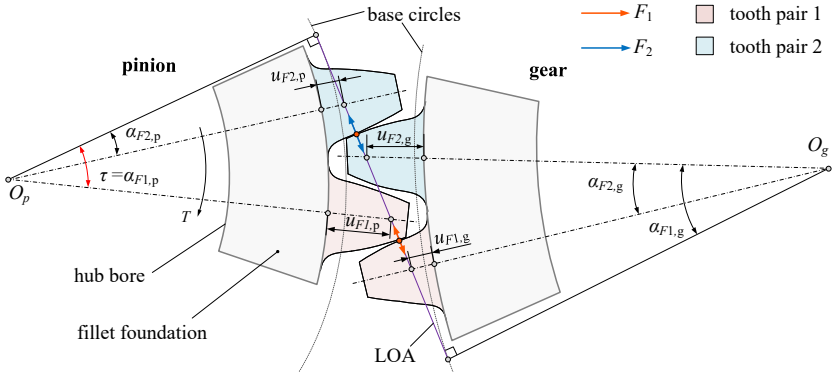


**Figure 5.** Configuration of a spur gear pair.

Based on involute geometry [31], for each tooth, the force action angle $\alpha_{Fi,j}$, in terms of $\tau$, can be explicitly expressed as follows:

$$\begin{aligned} &\alpha_{F1,p}(\tau) = \tau;\ \alpha_{F1,g}(\tau) = \frac{l_M}{R_{b,g}} - \left(\tau + \theta_{b,p}\right)\frac{R_{b,p}}{R_{b,g}} - \theta_{b,g}, \\ &\alpha_{F2,p}(\tau) = \tau - \frac{2\pi}{z_p};\ \alpha_{F2,g}(\tau) = \alpha_{F1,g}(\tau) + \frac{2\pi}{z_g} \end{aligned}, \tag{25}$$

where $l_M = \left(R_{b,\mathrm{p}} + R_{b,\mathrm{g}}\right)\tan\alpha_{\mathrm{n}}$ is the theoretical length of LOA ($\alpha_{\mathrm{n}}$ is the pressure angle), and $z$ is the tooth number.

Recalling Equation (9), the tooth deviation of each modified tooth (denoted as $e_{i,j}$) can be evaluated by the following:

$$e_{i,j}(\tau,\wp) = \frac{f_{\mathrm{T}}(\alpha_{Fi,j},\wp)}{\sqrt{\left(\alpha_{Fi,j}+\theta_{b,j}\right)^2+1}} + \varepsilon_{i,j}, i = 1,2;\ j = \mathrm{p},\mathrm{g}, \tag{26}$$

where $\varepsilon_{i,j}$ represents other types of tooth deviations (e.g., tooth wear and manufacturing errors). The total displacement error for tooth pair $i$, denoted as $e_i$, can be further expressed as follows:

$$e_i(\tau,\wp) = \sum_{j=p,g} e_{i,j}(\tau,\wp),\ i = 1,2. \tag{27}$$

Different spatial positions typically result in non-identical displacement errors of tooth pairs, namely $e_1(\tau,\wp) \neq e_2(\tau,\wp)$. Therefore, the displacement error of a freely rotating system (i.e., the spacing error) depends on the minimum value of $e_i, i = 1,2$:

$$E_{\mathrm{m}}(\tau,\wp) = \min\{e_1(\tau,\wp), e_2(\tau,\wp)\}, \tag{28}$$

where $E_{\mathrm{m}}(\tau,\wp)$ is the NSTE. We should note that the current work focuses on the early design of tip relief for high-precision gears, and $\varepsilon_{i,j}$ is approximated by $\varepsilon_{i,j} \approx 0$.

### *4.2. Evaluations of Mesh Stiffness and LSTE*

#### 4.2.1. Tooth Stiffness and Contact Stiffness

The tooth is typically idealized as a non-uniform cantilever beam. The tooth profile is simplified as purely involved with the boundary defined by the base circle [31,32]. The practical tooth profile starts from the root circle, together portrayed by transition curves and involute curves (see Figure 6a). Neglecting the flexibility of the transition region may induce noticeable calculation errors when the difference between the base and root circles arises. Although several studies [69–71] are devoted to this issue, classified formulas are required for different relative sizes between the base and root circles.

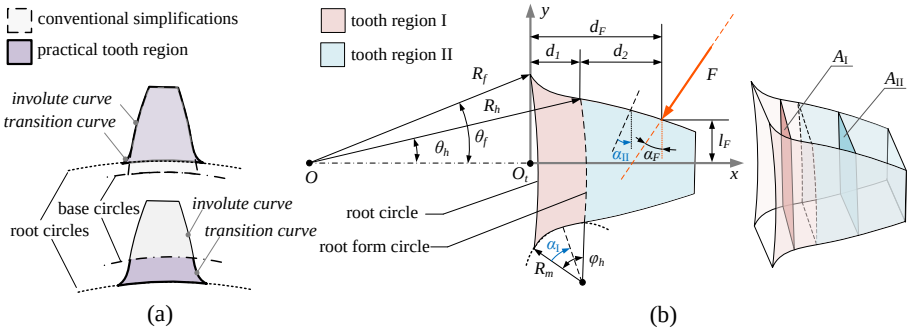


**Figure 6.** Sketch of tooth stiffness modeling: (**a**) tooth regions with different considerations. (**b**) A cantilever beam model with root circle boundary.

For more convenient tooth stiffness calculations, a unified tooth stiffness model is proposed. As depicted in Figure 6b, a local Cartesian coordinate system $\{x, O_t, y\}$ is defined at the root circle, and the origin $O_t$ is located at the tooth central line. Given a generic mesh force $F$ along the LOA with an action angle $\alpha_F$, the coordinate of the application point, $(d_F, l_F)$, can be expressed as follows:

$$d_F = R_b[(\theta_b+\alpha_F)\sin\alpha_F + \cos\alpha_F] - R_f\cos\theta_f,\ l_F = R_b[(\theta_b+\alpha_F)\cos\alpha_F - \sin\alpha_F], \tag{29}$$

where $R_f$ is the root circle radius, and $\theta_f$ is the half-tooth angle at the root circle. For a generic tooth with a root circle boundary, the transition region is defined as tooth region I (Figure 6b, red region) while the involute region is defined as tooth region II (Figure 6b, blue region). The border between tooth regions $r$ ($r = \mathrm{I}, \mathrm{II}$) is determined by the root form circle. In non-profile shifted conditions, the root form circle radius $R_h$ is as follows:

$$R_h = R_b \sec\left[\arctan\left(\tan\alpha_\mathrm{n} - \frac{4}{z\sin 2\alpha_\mathrm{n}}\right)\right]. \tag{30}$$

The potential energies stored in different tooth regions are as follows:

$$\frac{F^2}{2K_t} = U_t = \sum_{r=\mathrm{I,II}} U_{t,r} = \sum_{r=\mathrm{I,II}} (U_{a,r} + U_{b,r} + U_{s,r}), \tag{31}$$

where $K_t$ is the tooth stiffness; $U_t$ is the total potential energy stored in the cantilever beam; and $U_{a,r}$, $U_{b,r}$, and $U_{s,r}$ denote axial compression, the bending, and shearing energy stored in region $r$, respectively. By denoting $\mathbb{D}_r$ as the integral interval of tooth region $r$, expressions of potential energies $U_{a,r}$, $U_{b,r}$, and $U_{s,r}$ are summarized as follows:

$$U_{a,r} = \int_{\mathbb{D}_r}\left(\frac{F_x^2}{2EA_r}\right)dx,\ U_{b,r} = \int_{\mathbb{D}_r}\left(\frac{M_x^2}{2EI_r}\right)dx,\ U_{s,r} = \int_{\mathbb{D}_r}\left(\frac{1.2F_y^2}{2GA_r}\right)dx, \tag{32}$$

where $E$ represents Young's modulus, and $G = E/(1+\nu)/2$ is the shear modulus ($\nu$-the Poisson's ratio). $\{F_x, F_y\} = \{F\sin\alpha_F, F\cos\alpha_F\}$, respectively, denote orthogonal components of mesh force $F$ along the $x, y$ axis, and $M_x = F_y(d_F - x) - F_x l_F$ is the bending moment. $A_r$ and $I_r$ are the cross-sectional area and the moment of inertia for tooth region $r$ ($r = \mathrm{I}, \mathrm{II}$), respectively.

For tooth region I, the integral interval satisfies $\mathbb{D}_r = [0, d_1]$. Generally, the transition curve is a prolate involute with the minimum curvature radius $R_m$ (i.e., the fillet radius) generated by the round corner of the cutting tool. Strict geometrical descriptions on the prolate involute curve would be mathematically tedious. To avoid such complicated expressions in practice while capturing potential energies stored in different tooth regions, the transition curve is approximated by a circular arc with the radius $R_m$. Letting the central angle $\alpha_\mathrm{I}$ be the integral variant, $A_r$ and $I_r$ ($r = \mathrm{I}$) in terms of $\alpha_\mathrm{I}$ are as follows:

$$\begin{aligned} A_\mathrm{I}(\alpha_\mathrm{I}) &= 2LR_f\left[\left(1+\frac{R_m}{R_f}\right)\sin\theta_f - \frac{R_m}{R_f}\sin\left(\theta_f + \alpha_\mathrm{I}\right)\right]; \\ I_\mathrm{I}(\alpha_\mathrm{I}) &= \frac{2}{3}LR_f^3\left[\left(1+\frac{R_m}{R_f}\right)\sin\theta_f - \frac{R_m}{R_f}\sin\left(\theta_f + \alpha_\mathrm{I}\right)\right]^3. \end{aligned} \tag{33}$$

For tooth region II, the integral interval follows $\mathbb{D}_r = [d_1, d_2]$. The angular parameter $\alpha_\mathrm{II}$ is introduced. If force direction deviation and tooth strength reduction caused by micro-sized material removals are negligible, $A_r$ and $I_r$ ($r = \mathrm{II}$) in terms of $\alpha_\mathrm{II}$ hold:

$$\begin{aligned} A_\mathrm{II}(\alpha_\mathrm{II}) &= 2LR_b[\sin\alpha_\mathrm{II} + (\theta_b - \alpha_\mathrm{II})\cos\alpha_\mathrm{II}] \\ I_\mathrm{II}(\alpha_\mathrm{II}) &= \frac{2}{3}LR_b^3[\sin\alpha_\mathrm{II} + (\theta_b - \alpha_\mathrm{II})\cos\alpha_\mathrm{II}]^3. \end{aligned} \tag{34}$$

Substituting Equations (33) and (34) into Equation (32), one obtains the following:

$$\begin{aligned}\frac{1}{K_{a,r}} &= \int_{\mathbb{D}_r} \frac{\Lambda_{a,r}(\alpha_r)\sin^2\alpha_F}{2EL\Omega_r(\alpha_r)}d\alpha_r \\ \frac{1}{K_{b,r}} &= \int_{\mathbb{D}_r} \frac{\Lambda_{b,r}(\alpha_F,\alpha_r)\cos^2\alpha_F}{2EL\Omega_r^3(\alpha_r)}d\alpha_r, \\ \frac{1}{K_{s,r}} &= \int_{\mathbb{D}_r} \frac{\Lambda_{s,r}(\alpha_r)\cos^2\alpha_F}{2GL\Omega_r(\alpha_r)}d\alpha_r\end{aligned} \tag{35}$$

where non-dimensional terms $\Lambda_{a,r}, \Lambda_{b,r}, \Lambda_{s,r}, \Omega_r$, and $\mathbb{D}_r(\alpha_r)$ are summarized in Appendix A. Combining Equations (31) and (35), the tooth stiffness $K_t$ follows:

$$\frac{1}{K_t} = \sum_{r=\mathrm{I,II}} \left( \frac{1}{K_{a,r}} + \frac{1}{K_{b,r}} + \frac{1}{K_{s,r}} \right). \tag{36}$$

For a certain tooth $i$ of pinion ($j = \mathrm{p}$) or gear ($j = \mathrm{g}$), one can append subscripts $i, j$ to Equations (30)–(36) to calculate the corresponding tooth stiffness $K_{ti,j}$.

Apart from combined deformations caused by mesh force $F$, contact compliances between tooth interfaces arise. To capture the load-dependent contact stiffness of the tooth pair, the semi-empirical formula [72] is adopted:

$$K_h = \frac{F}{\delta_h} = \frac{E^{0.9}L^{0.8}F^{0.1}}{1.275}, \tag{37}$$

where $K_h$ is the Hertzian contact stiffness of a generic tooth pair; $\delta_h$ is the contact compliance of tooth pair.

#### 4.2.2. Fillet Foundation Stiffness

For the fillet foundation stiffness calculation, Sainost's formulas [33] and Xie's formulas [34] are frequently adopted. Essentially, these formulas [33,34] are curve-fitted polynomials in plane strain, limited by ranges of geometric parameters (e.g., $\theta_f$ and $R_f/R_{\mathrm{int}}$, $R_{\mathrm{int}}$-the hub bore radius) and the plane stress (e.g., thin-walled gears). To remove such restrictions, previous works [59,60] developed asymptotic forms of fillet foundation stiffness and provided a fast computational strategy, which is further integrated into the current study.

Alternating tooth engagements result in different loading patterns and change the deformation responses of the fillet foundation. In single-tooth contact (STC), merely the local mesh force from the engaged tooth $i$ deforms the fillet foundation, and the resistance of tooth deflection induced by the fillet foundation is described by the following:

$$\frac{1}{K_{fii}} = \frac{\cos^2\alpha_{Fi}}{EL}\left[\Psi_0(\kappa)\cdot\left(\frac{u_{Fi}}{S_f}\right)^0 + \Psi_1(\kappa)\cdot\left(\frac{u_{Fi}}{S_f}\right)^1 + \Psi_2(\kappa)\cdot\left(\frac{u_{Fi}}{S_f}\right)^2\right], \tag{38}$$

where $K_{fii}$ is the corresponding fillet foundation stiffness component for tooth $i$; $S_f = 2\theta_f R_f$ is the arc length of the junction between tooth and foundation, and $u_{Fi}$ denotes the moment arms of mesh forces to the corresponding junctions (see Figure 4). For simultaneous tooth contact, mesh forces from adjacent teeth induce additional deformations of fillet foundation, and the corresponding resistances of tooth deflections hold:

$$\begin{cases} \dfrac{1}{K_{f21}} = \dfrac{\cos\alpha_{F1}\cos\alpha_{F2}}{EL}\left[\Theta_0^{2,1}(\kappa) + \Theta_1^{2,1}(\kappa)\cdot\dfrac{u_{F1}}{S_f} + \Theta_2^{2,1}(\kappa)\cdot\dfrac{u_{F2}}{S_f} + \Theta_3^{2,1}(\kappa)\cdot\dfrac{u_{F1}u_{F2}}{S_f^2}\right] \\ \dfrac{1}{K_{f12}} = \dfrac{\cos\alpha_{F1}\cos\alpha_{F2}}{EL}\left[\Theta_0^{1,2}(\kappa) + \Theta_1^{1,2}(\kappa)\cdot\dfrac{u_{F2}}{S_f} + \Theta_2^{1,2}(\kappa)\cdot\dfrac{u_{F1}}{S_f} + \Theta_3^{1,2}(\kappa)\cdot\dfrac{u_{F1}u_{F2}}{S_f^2}\right] \end{cases}, \tag{39}$$

where $K_{f21}$ is the deformation resistance of tooth 2 to the mesh force $F_1$; $K_{f12}$ is the deformation resistance of tooth 1 to the mesh force $F_2$. Dimensionless coefficients $\Psi_{s=0,1,2}$, $\Theta^{2,1}_{s=0,1,2,3}$, and $\Theta^{1,2}_{s=0,1,2,3}$ are linked to Kolosov's constant $\kappa$. According to the Cornell criterion [73], the choice of Kolosov's constant $\kappa$ follows:

$$\begin{cases} \text{Thick}-\text{walled}: \ 2L/\pi m > 5, \ \kappa = 3 - 4\nu \\ \text{Thin}-\text{walled}: \ 2L/\pi m < 5, \ \kappa = \dfrac{3-\nu}{1+\nu} \end{cases}, \tag{40}$$

where $\nu$ denotes Poisson's ratio. For detailed evaluations of $\Psi_{s=0,1,2}$, $\Theta^{2,1}_{s=0,1,2,3}$, and $\Theta^{1,2}_{s=0,1,2,3}$ see Ref. [59].

#### 4.2.3. Mesh Stiffness and LSTE

This section further evaluates the mesh stiffness and LSTE. Figure 7 pre-defines mesh intervals within one complete mesh cycle ($\tau \in [\beta_1, \beta_4]$), where tooth pair 1 is initialized at the pitch point ($\tau = \beta_1$). For unmodified spur gear pairs, theoretical single-tooth contact (STC) and double-tooth contact (DTC) successively occur within the mesh cycle (black curves in Figure 7). Theoretical mesh intervals can be readily defined with $\beta_{1,2,3,4}$ by involute geometry. As indicated in Ref. [59], due to the ETC effect, tooth separation distances between mesh pairs induce smooth transitions between theoretical STC and DTC (blue curves in Figure 7).

Situations are more complicated for modified cases. The ETC effect and tooth deviations caused by tip relief jointly influence deformation compatibilities, resulting in different types of boundaries of simultaneous tooth contact (i.e., $\varphi_1$ and $\varphi_2$). For cases with large modification amounts and small torques (red curves in Figure 7a), $\varphi_1$, $\varphi_2$ are located within the interval $(\beta_2, \beta_3)$, since enough spacing errors are created to delay onsets of simultaneous tooth contact. Conversely, $\varphi_1$, $\varphi_2$ would be shifted beyond the interval $(\beta_2, \beta_3)$, resulting in additional smooth transitions (red curves in Figure 7b).

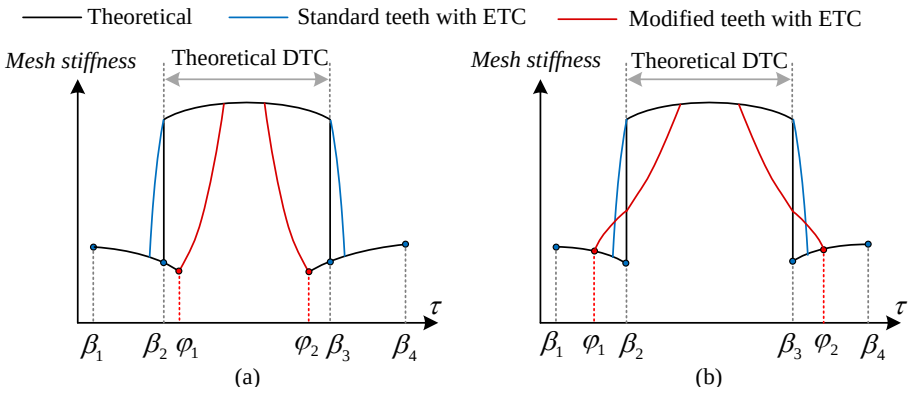


**Figure 7.** Schematic of mesh stiffness curves and intervals for modified spur gears under different cases: (**a**) the case of large modification amounts or small torques; (**b**) the case of insufficient modification amounts or large torques.

By denoting $\delta_{i,j}$ as the elastic mesh deflection of tooth $i$ for pinion ($j = \mathrm{p}$) and gear ($j = \mathrm{g}$), the relation between deflections and deviations in simultaneous tooth contact holds:

$$\sum_{j=\mathrm{p,g}} \left[\delta_{2,j}(\tau, F_1, F_2, \wp) - \delta_{1,j}(\tau, F_1, F_2, \wp) + e_{2,j}(\tau, \wp) - e_{1,j}(\tau, \wp)\right] + R_{b,\mathrm{p}}\Phi(\tau) = 0, \tag{41}$$

where $\Phi(\tau)$ is the angular tooth separation distance, indicating the angular distance that separates two standard involute teeth before they come into contact [74]. Within the mesh cycle $\tau \in [\beta_1, \beta_4]$, the function $\Phi(\tau)$ satisfies the following:

$$\Phi(\tau) = 0,\ \tau \in (\beta_2, \beta_3);\ \Phi(\tau) \neq 0,\ \tau \in [\beta_1, \beta_2] \cup [\beta_3, \beta_4]. \tag{42}$$

Explicit expressions of $\Phi(\tau)$ can be found in Ref. [59]. Complicated boundaries in Figure 7a,b share the same scenario, where a certain tooth pair is engaged and another tooth pair is just in touch with zero mesh forces. Therefore, assigning $F_1 = 0$ or $F_2 = 0$ into Equation (41) and noticing $F_1 + F_2 = T/R_{b,\mathrm{p}}$, one obtains equations of boundaries $\varphi_1$ and $\varphi_2$:

$$\begin{cases} \sum\limits_{j=\mathrm{p,g}} \left[ \delta_{2,j}\left(\varphi_1, \dfrac{T}{R_{b,\mathrm{p}}}, 0, \wp\right) - \delta_{1,j}\left(\varphi_1, \dfrac{T}{R_{b,\mathrm{p}}}, 0, \wp\right) + e_{2,j}(\varphi_1, \wp) - e_{1,j}(\varphi_1, \wp) \right] = -R_{b,p}\Phi(\varphi_1) \\ \sum\limits_{j=\mathrm{p,g}} \left[ \delta_{2,j}\left(\varphi_2, 0, \dfrac{T}{R_{b,\mathrm{p}}}, \wp\right) - \delta_{1,j}\left(\varphi_2, 0, \dfrac{T}{R_{b,\mathrm{p}}}, \wp\right) + e_{2,j}(\varphi_2, \wp) - e_{1,j}(\varphi_2, \wp) \right] = -R_{b,p}\Phi(\varphi_2) \end{cases}. \tag{43}$$

Recalling Equations (36)–(39), explicit forms of $\delta_{i,j}$ in terms of $F_1$ and $F_2$ hold:

$$\begin{cases} \sum\limits_{j=\mathrm{p,g}} \delta_{1,j}(\tau, F_1, F_2, \wp) = F_1 \sum\limits_{j=\mathrm{p,g}} \left( \dfrac{1}{K_{t1,j}} + \dfrac{1}{K_{f11,j}} + \dfrac{1}{2K_{h1}} \right) + F_2 \sum\limits_{j=\mathrm{p,g}} \dfrac{1}{K_{f12,j}} \\ \sum\limits_{j=\mathrm{p,g}} \delta_{2,j}(\tau, F_1, F_2, \wp) = F_2 \sum\limits_{j=\mathrm{p,g}} \left( \dfrac{1}{K_{t2,j}} + \dfrac{1}{K_{f22,j}} + \dfrac{1}{2K_{h2}} \right) + F_1 \sum\limits_{j=\mathrm{p,g}} \dfrac{1}{K_{f21,j}} \end{cases}. \tag{44}$$

Combining Equations (41)–(44), one can numerically solve mesh forces $F_1$, $F_2$ and boundary values $\varphi_1$, $\varphi_2$.

The loaded static transmission error (LSTE) is a linear combination of mesh deflections and tooth deviations, which can further be calculated by the following:

$$\delta_{\mathrm{m}}(\tau, T, \wp) = \sum_{j=\mathrm{p,g}} \delta_{i,j}(\tau, F_1, F_2, \wp) + \sum_{j=\mathrm{p,g}} e_{i,j}(\tau, \wp) = \delta_i(\tau, F_1, F_2, \wp) + e_i(\tau, \wp),\ i = 1, 2, \tag{45}$$

where $\delta_i = \delta_{i,\mathrm{p}} + \delta_{i,\mathrm{g}}$ and $e_i = e_{i,\mathrm{p}} + e_{i,\mathrm{g}}$ are the resultant mesh deflection and deviation of tooth pair $i$, respectively.

For mesh stiffness calculation, NSTE should be excluded. Combining Equation (28) and Equation (45), the mesh stiffness $K_{\mathrm{m}}$ is given by the following:

$$K_{\mathrm{m}}(\tau, T, \wp) = \frac{T/R_{b,\mathrm{p}}}{\delta_{\mathrm{m}}(\tau, T, \wp) - E_{\mathrm{m}}(\tau, \wp)}. \tag{46}$$

In summary, Section 4 proposes an analytical model of mesh excitations, which comprehensively embodies various geometric features and load-dependent mesh intervals.

### *4.3. Flowchart of Tip Relief Modeling and Design*

To clarify, the flowchart of the current framework is modularized in Figure 8, comprising the evaluation module (based on Section 4) and the design module (based on Section 3).

The evaluation module (see Figure 8a) aims to provide mesh excitations (mesh stiffness, LSTE, and NSTE) at each grid of the map predefined by Equation (13). Without loss of generality, at each grid, mesh excitations within two complete mesh cycles are calculated, where the mesh duration $\tau \in [\beta_1, 2\beta_4 - \beta_1]$ is discretized into 200 points.

In the design module (see Figure 8b), parallel computing based on the predefined map is further performed to prepare enough mesh excitation data for tip relief design. Next, double-searching (see Section 3.2 for details) is performed in the design module to sort suitable tip relief configurations at target working conditions. After examinations of gear dynamics, the flowchart further outputs meshing properties (see Figure 8c) with sorted configurations $\wp^*$. To reflect the independent correlations between tip relief and mesh mechanism, NSTE caused by manufacturing tolerance, wear, and fracture are excluded in

the current case study, which could be further integrated into the present method based on experiments.

All numerical computations are based on a 4 GHz quad-core CPU with 32 GB of RAM. Computation time is estimated with the 'tic-toc' function of Matlab® (version: R2024b; MathWorks, Inc.; Natick, MA, USA). For the evaluation of mesh excitations (including mesh stiffness, LSTE, and NSTE) at a given applied torque over two mesh cycles (200 data points), the proposed analytical model requires about 2–3 s, greatly reducing computational time compared to the benchmark FEM model (10–12 min). Moreover, parallel computing further accelerates computations in the design stage. For design cases in this paper ($40 \times 40$ data sets of mesh excitations), the average computational effort of the whole procedure is around 12–15 min.

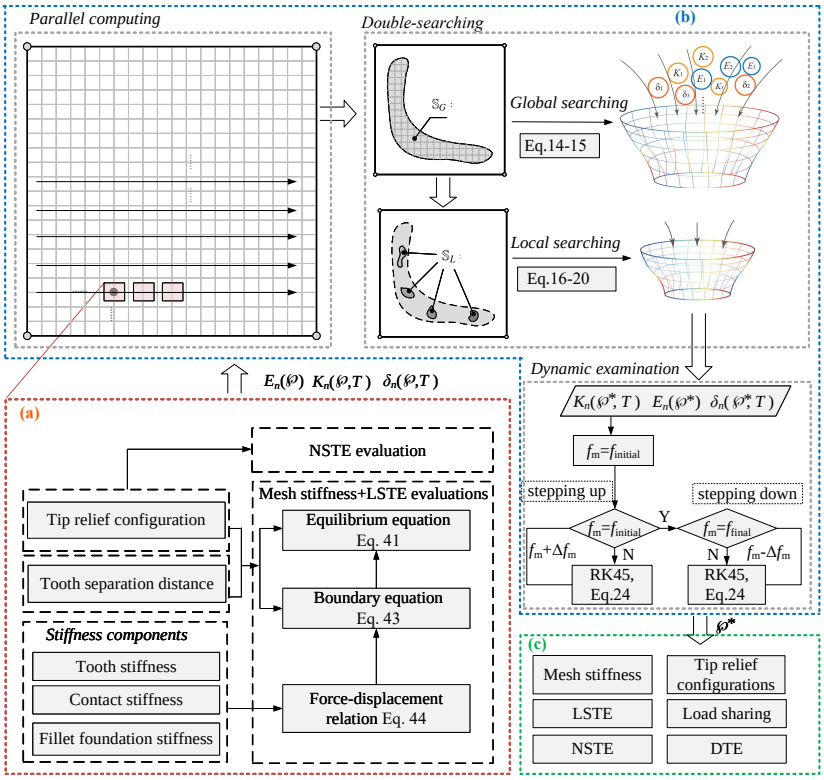


**Figure 8.** Flowchart of tip relief modeling and design: (**a**) Evaluation module; (**b**) design module; (**c**) results of design.

## 5. Verifications

### *5.1. Verification of Deformation Responses*

This section compares predicted deformation responses with FEM results, including mesh stiffness, load sharing, and LSTE. To check the flexibilities of the proposed model in dealing with various geometric features (thick/thin-walled cases, different tooth regions), two types of spur gear pairs (labeled as gear pair A and B with parameters see Appendix B) are specially selected with considerations as follows:

- Gear pair A satisfies the thick-walled case (plane strain, $2L/\pi m > 5$). The tooth region follows the case $R_b > R_f$ (see Figure 6a). FEM results from Ma et al. [56] (plane strain elements, ANSYS ® (ANSYS, Inc.; Canonsburg, PA, USA)) are adopted as benchmarks.
- Gear pair B is a thin-walled case (plane stress, $2L/\pi m < 5$). The region tooth follows the case $R_b < R_f$. The 2D FE models with CPS4R elements (plane stress elements, Abaqus® (version: 2016; Dassault Systèmes; Paris, France)) are established for supplementary comparisons (see Appendix C for details).

The most representative modification shape—linear tip relief—is included in the comparisons.

Figure 9 compares mesh stiffness curves of gear pair A between FEM [56] and the proposed model, showing close results under different conditions. Due to progressively trimmed tooth profiles along tooth depths, the rising $L_{\mathrm{n}}$ gradually narrows simultaneous tooth contact regions in Figure 9a,d. $C_{\mathrm{n}}$ dictates magnitudes of tooth deviations during mesh, shaping the transition curves in Figure 9b,e. Moreover, the increasing $T$ enlarges the coupling deformations ($\delta_{f12}$ and $\delta_{f21}$), trending to bring forward tooth engagement-in and delay tooth engagement-out. Consequently, increased regions of simultaneous tooth contact are reflected in both FEM and the proposed model (Figure 9c,f).

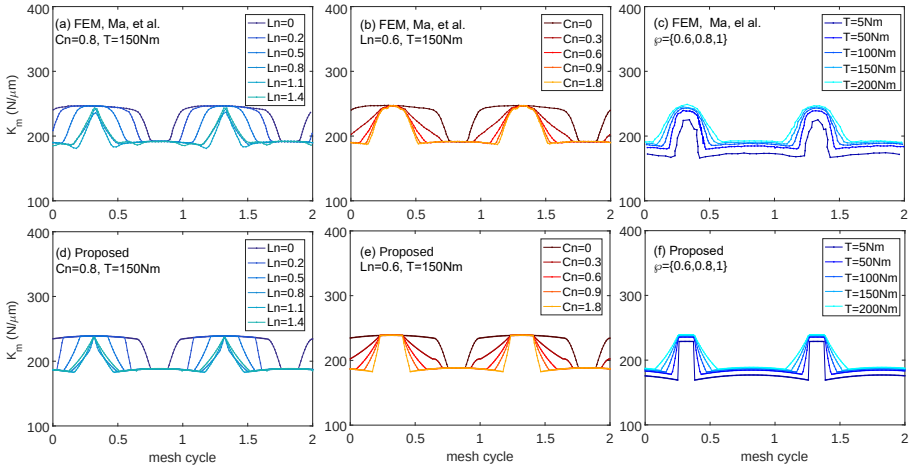


**Figure 9.** Mesh stiffness obtained by FEM and the proposed model for gear pair A with linear tip relief (thick-walled, tooth region $R_b > R_f$, $R_{\mathrm{int}} = 6.3$ mm): (**a**–**c**) FEM results digitized from Ref. [56] (plane strain elements); (**d**–**f**) plane strain solutions by the proposed model.

Likewise, mesh stiffness curves of gear pair B are compared in Figure 10. Again, good correspondences between FEM (Figure 10a–c) and the proposed model (Figure 10d–f) are observed. For small levels of $C_{\mathrm{n}}$ (e.g., Figure 10c,f, $C_{\mathrm{n}} = 0.1$), tooth deviations and nonzero tooth separation distance jointly influence deformation compatibilities, creating additional smooth transitions in FEM (Figure 10c) and the proposed model (Figure 10f).

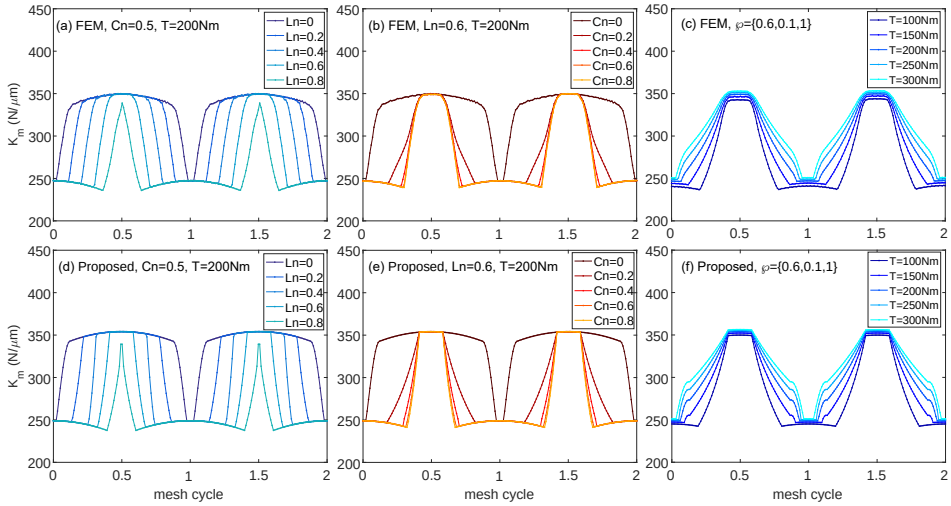


**Figure 10.** Mesh stiffness obtained by FEM and the proposed model for gear pair B with linear tip relief (thin-walled, tooth region $R_b < R_f$, $R_{\mathrm{int}} = 30$ mm): (**a**–**c**) FEM results with CPS4R (plane stress elements); (**d**–**f**) plane stress solutions by the proposed model.

Figure 11 shows the load sharing of gear pair B where the load sharing ratio of tooth pair 2 (namely, $F_2R_{b,\mathrm{p}}/T$) is adopted as an example. For different modification lengths $L_\mathrm{n}$ (Figure 11a,d), modification amounts $C_\mathrm{n}$ (Figure 11b,e), and applied torques $T$ (Figure 11c,f), the proposed solutions match well with the simulation results.

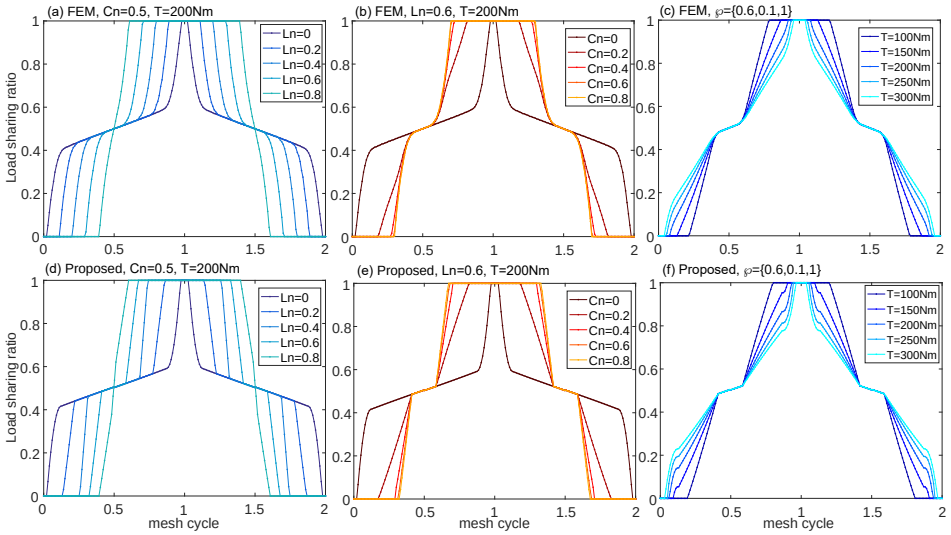


**Figure 11.** Load sharing ratios obtained by FEM and the proposed model for gear pair B with linear tip relief (thin-walled, tooth region $R_b < R_f$, $R_\mathrm{int} = 30$ mm): (**a**–**c**) FEM results with CPS4R (plane stress elements); (**d**–**f**) plane stress solutions by the proposed model.

Figure 12a exhibits LSTE waveforms (4-order Fourier representations) of gear pair B obtained by the proposed model (continuous lines) and FEM (dashed lines), where $\wp = \{0.6, 0.1, 1\}$ and $T = 100{-}300$ Nm. The results show that the proposed model and FEM present close shapes and magnitudes of LSTE waveforms under different levels of $T$, where the relative error ranges 0.22–5.02%.

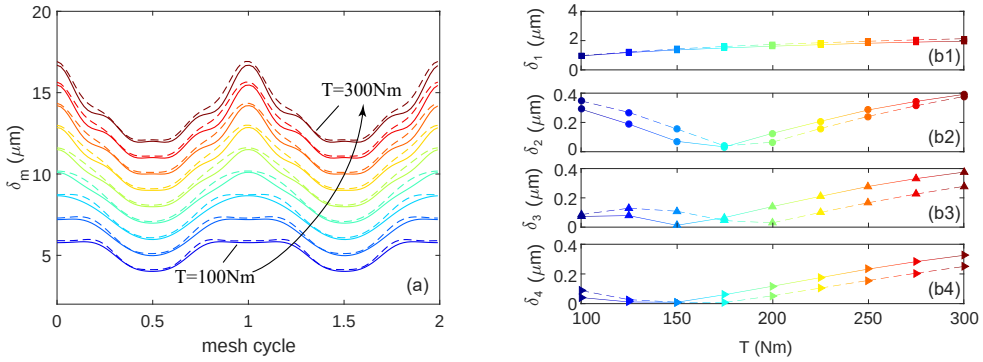


**Figure 12.** Comparisons of the LSTE between the proposed model (continuous lines, '—') and FEM (dashed lines, '- - -') for gear pair B ($\wp = \{0.6, 0.1, 1\}$, $T = 100{-}300$Nm, spacing $\Delta T = 25$ Nm): (**a**) 4th-order Fourier representation of $\delta_\mathrm{m}$; (**b1**–**b4**) harmonic contents $\delta_1$–$\delta_4$.

Figure 12(b1)–(b4) further compares the corresponding harmonic contents $\delta_n$. Due to simplifications in the proposed model and discretization in FE modeling, quantitative discrepancies still exist in this more detailed comparison. Nevertheless, even for higher orders ($n = 3, 4$), both results present the consistent monotonicity of $\delta_n - T$ curves, showing acceptable accuracies of the proposed model in capturing the load-dependent harmonic contents.

### 5.2. Verification of Dynamic Responses

To check the feasibility of the current model in vibration analyses, the results are compared with experimental data [64], where the DTE of gear pair B with linear tip relief is measured. The equivalent RMS (root-mean-square) of the oscillating DTE component is adopted as an indicator [64], i.e., $A_{\mathrm{rms}} = \sqrt{\sum_{n=1}^{3} A_n^2}$ ($A_n$-the $n^{\mathrm{th}}$ harmonic amplitude of DTE).

Figure 13 compares the $A_{\mathrm{rms}}$ of gear pair B ($T = 340$ Nm) between the proposed model and experiments. The testing speed range varies from 600 to 4100 rpm ($f_{\mathrm{m}} \approx 500$–$3400$ Hz). The modification length is described by the starting roll angle $\alpha_{\mathrm{roll}}$ in the test: $\alpha_{\mathrm{roll}} = 20.9^\circ, 22.2^\circ, 23.6^\circ, 24.8^\circ$ (namely, $L_{\mathrm{n}} \approx 1.67, 1.36, 1.00, 0.68$), and the modification amount is $C_T = 10$ μm ($C_{\mathrm{n}} \approx 0.17$). Following the original presentation in Ref. [64], the abscissa is normalized by the ratio between the mesh frequency $f_{\mathrm{m}}$ and the natural frequency $f_{\mathrm{n}}$. Due to inherent limitations of SDOF assumptions and uncertainties of manufacturing/measurement in nature, local discrepancies still exist. Nevertheless, for each tip relief case in Figure 13a–d, the proposed model reproduces the experimental amplitudes and frequencies with reasonable accuracy. Moreover, softening-type jumps and saddle-node bifurcations caused by single-sided tooth impacts (SSIs) are well-captured.

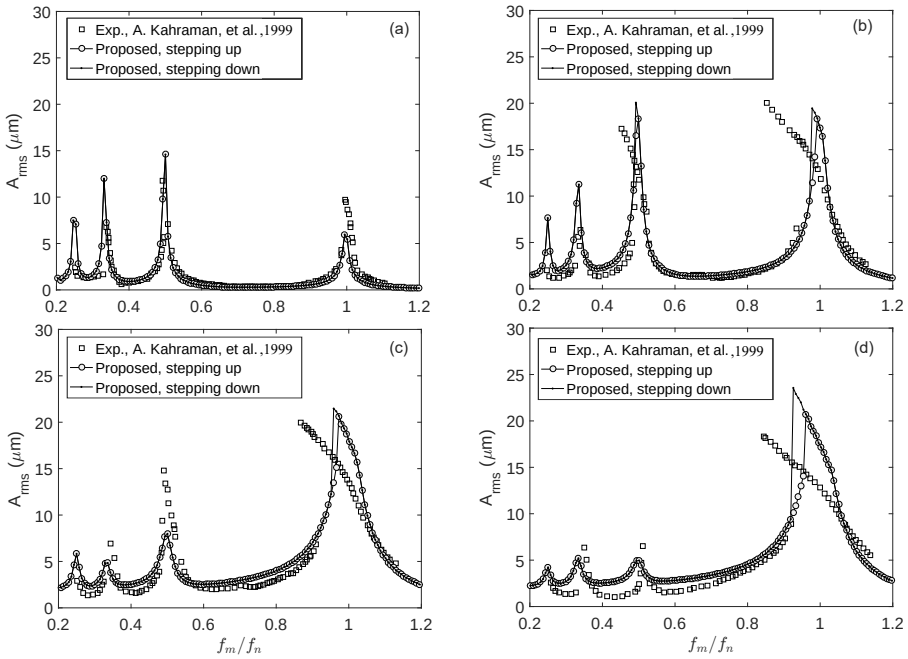


**Figure 13.** $A_{\mathrm{rms}}$ of gear pair B ($T = 340$ Nm, $R_{\mathrm{int}} = 22.5$ mm, $C_{\mathrm{T}} = 10$ μm) reproduced by the proposed model and experiments [64] with different starting roll angles for tip relief: (**a**) $\alpha_{\mathrm{roll}} = 20.9^\circ$; (**b**) $\alpha_{\mathrm{roll}} = 22.2^\circ$; (**c**) $\alpha_{\mathrm{roll}} = 23.6^\circ$; (**d**) $\alpha_{\mathrm{roll}} = 24.8^\circ$.

Figure 13a–d also indicate that tip relief can significantly alter relative amplitudes of primary ($f_{\mathrm{m}}/f_{\mathrm{n}} = 1$) and super-harmonic resonances ($f_{\mathrm{m}}/f_{\mathrm{n}} = 1/2, 1/3, \ldots$). As $\alpha_{\mathrm{roll}}$ changes, similar varying patterns of multi-resonance peaks between numerical results and experimental results are observed, showing the effectiveness of the proposed model in capturing the sensitivity of gear dynamics to tip relief parameters.

In terms of the fundamental vibration component $A_1$, comparison results in Figure 14a,b again confirm the above indication. Both upper and lower branches of $A_1$ curves evidently change with $\alpha_{\mathrm{roll}}$. In the condition of $T = 340$ Nm, as the overall level of upper/lower branches ascends, both the proposed model and experiments share the same varying route of parameter $\alpha_{\mathrm{roll}}$, namely $\alpha_{\mathrm{roll}} = 20.9^\circ \rightarrow 22.2^\circ \rightarrow 23.6^\circ \rightarrow 24.8^\circ$.

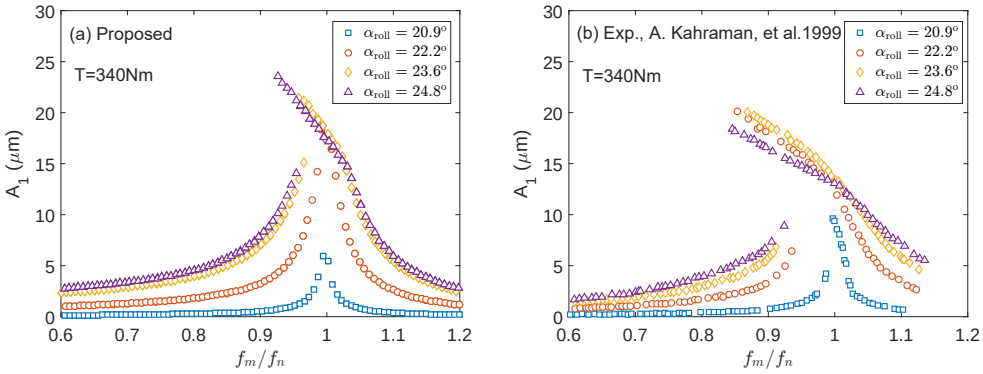


**Figure 14.** $A_1$ of gear pair B ($T = 340$ Nm, $R_{int} = 22.5$ mm, $C_T = 10$ µm) with different starting roll angles, $\alpha_{roll}$, for tip relief: (**a**) the proposed model; (**b**) experiments [64].

Interestingly, as reflected in both the proposed model (Figure 15a) and experiments (Figure 15b), if the applied torque is reduced to $T = 170$ Nm, the varying route entirely differs from the former case ($T = 340$ Nm), which becomes $\alpha_{roll} = 22.2° \rightarrow 20.9° \rightarrow 23.6° \rightarrow 24.8°$. In that light, it further demonstrates the capability of the proposed model to track the load dependency of modified spur gears in dynamic analysis.

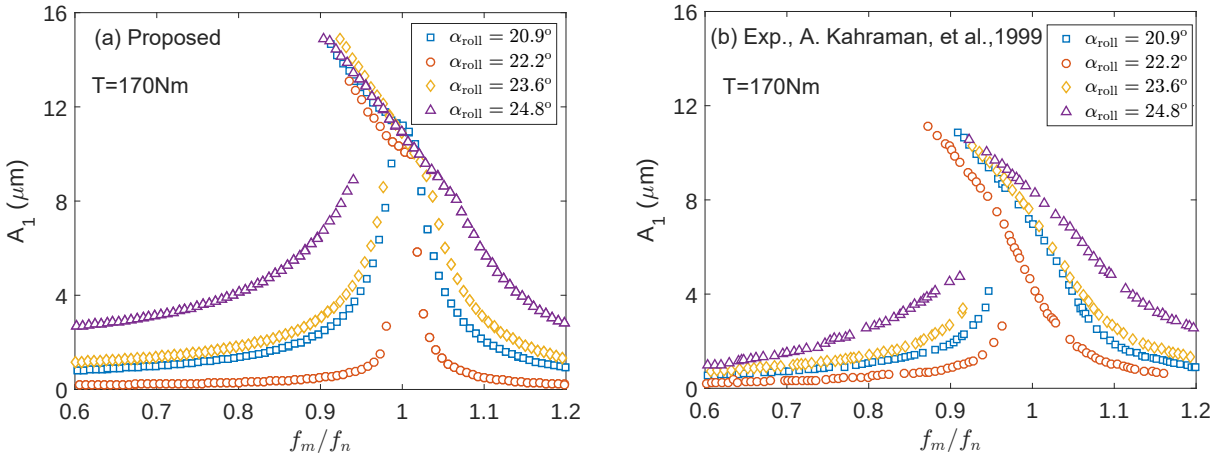


**Figure 15.** $A_1$ of gear pair B ($T = 170$ Nm, $R_{int} = 22.5$ mm, $C_T = 10$ µm) with different starting roll angles, $\alpha_{roll}$, for tip relief: (**a**) the proposed model; (**b**) experiments [64].

From quasi-statics (Section 5.1) to dynamics (Section 5.2), comparisons with FEM and experiments indicate reasonable accuracy in predicting the deformation and vibration of modified spur gears, laying the foundation for subsequent parametric studies.

## 6. Parametric Studies

Parametric studies are performed in this section, where gear pair B is selected for the case study. Section 6.1 explores harmonic correlations between LSTE and DTE. Application examples of the proposed design method are further discussed in Section 6.2.

### *6.1. Harmonic Correlations Between LSTE and DTE*

Figure 16 shows overviews of LSTE waveforms (Figure 16a–c, 4th-order Fourier waveforms) and DTE (Figure 16d–f, $A_{rms}$ values) under wide ranges of multi-parameters (i.e., $L_n \in [0, 1.5]$, $C_n \in [0, 1.5]$, and $T \in [100, 300]$ Nm). Figure 16a–c show that both tip relief parameters and applied torques evidently change LSTE waveforms. The different material removal patterns of $L_n$ and $C_n$ result in distinct variation trends of LSTE waveforms in Figure 16a,b. On the other hand, the increment of $T$ enlarges elastic deformations and

extends simultaneous tooth contact intervals, resulting in an upward trend and varying waveform shapes in Figure 16c.

The changed LSTE waveforms further excite different vibration responses in Figure 16d–f. For high levels of $L_n$ and $C_n$, the increasing spacing errors induce a climb-up trend in the $A_{rms}$ curves in Figure 16d,e. In addition, the potential energies of the vibration system increase with the applied torque $T$, enlarging the overall level of $A_{rms}$ in Figure 16f. Asynchronous distributions of multiple peaks in Figure 16d–f also reflect that harmonic resonances are sensitive to both tip relief parameters and applied torques.

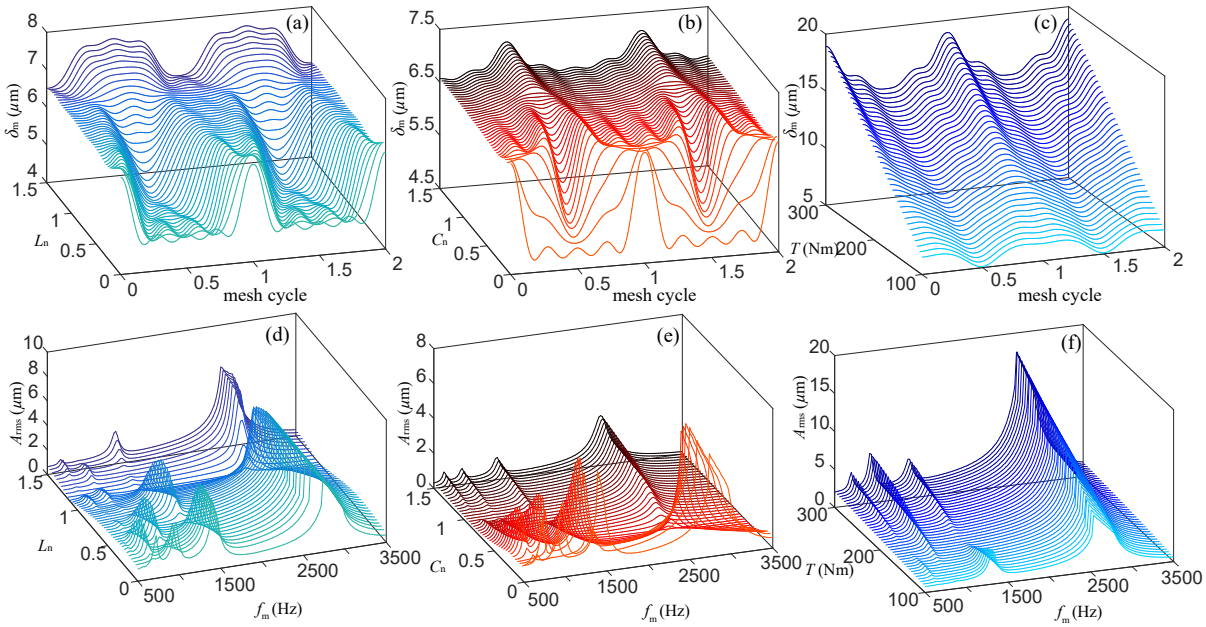


**Figure 16.** Overview of the LSTE and DTE under different tip relief parameters $L_n$, $C_n$, and applied torque $T$ for gear pair B: (**a**–**c**) 4th-order Fourier waveforms of $\delta_m$; (**d**–**f**) $A_{rms}$ curves in stepping up process.

Figure 17 further displays the corresponding harmonic contents of DTE, namely $A_{n=1,2,3,4}$. Peak values of $A_n$ are tracked with red points. With changes in $L_n$ and $C_n$, "V" shapes of the fundamental vibration component $A_1$ can be observed in Figure 17(a1),(b1). Situations become more complicated for higher-order cases, presenting multiple "V" shapes of $A_n, n = 2, 3, 4$ curves (see Figure 17(a2)–(a4),(b2)–(b4)). The sensitive variations are closely correlated with the load-dependent mesh intervals and transitions. Even for the same tip relief parameters, $A_1$–$A_4$ sharply change with the applied torque (Figure 17(c1)–(c4)).

Figures 16 and 17 indicate that LSTE is sensitive to tip relief at different working conditions and further excites complicated spectrums of DTE. However, deeper correlations between LSTE and DTE are still unclear at present. To this end, Figure 18 further compares the corresponding harmonic contents, namely $\delta_{n=1,2,3,4}$ (left vertical axis) and $A_{n=1,2,3,4}$ (right vertical axis, peak values). With changes in both tip relief parameters and loading conditions, each order of harmonic content presents similar variation trends and monotonicity. Moreover, the shapes of the $\delta_n$ and $A_n$ curves show high consistency, confirming the presupposition in Equation (7), namely, $\delta_n(\wp, T) \propto A_n(\wp, T)$, $n = 1, 2, 3, 4$.

Through extensive parametric analyses, it can be concluded that the LSTE and DTE are strongly correlated and share close harmonic characteristics. More importantly, observations in Figure 18 further demonstrate the feasibility of the proposed method in Section 3.2, laying foundations for the subsequent applications of tip relief design.

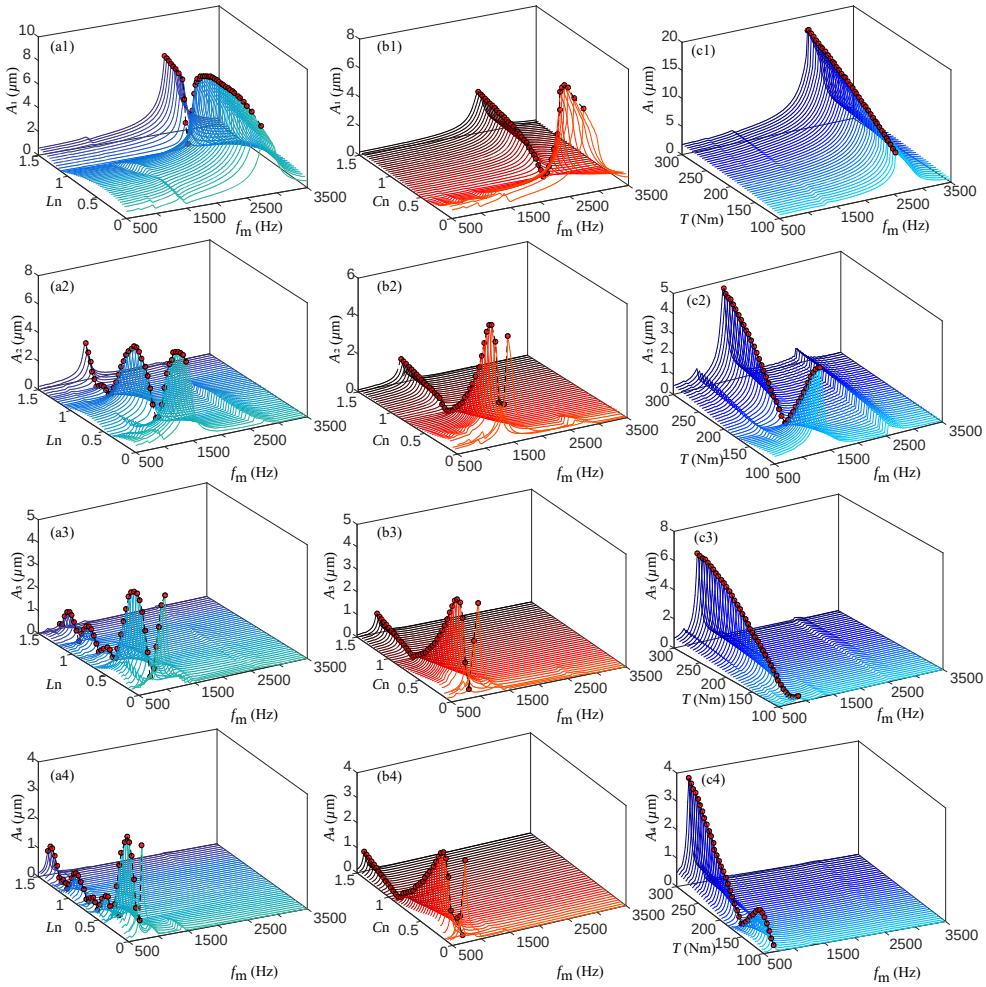


**Figure 17.** Spectrum of $A_{n=1,2,3,4}$ for gear pair B: (**a1–a4**) $A_n$ spectrums with different modification length $L_n$; (**b1–b4**) $A_n$ spectrums with different modification amount $C_n$; (**c1–c4**) $A_n$ spectrums with different applied torque $T$.

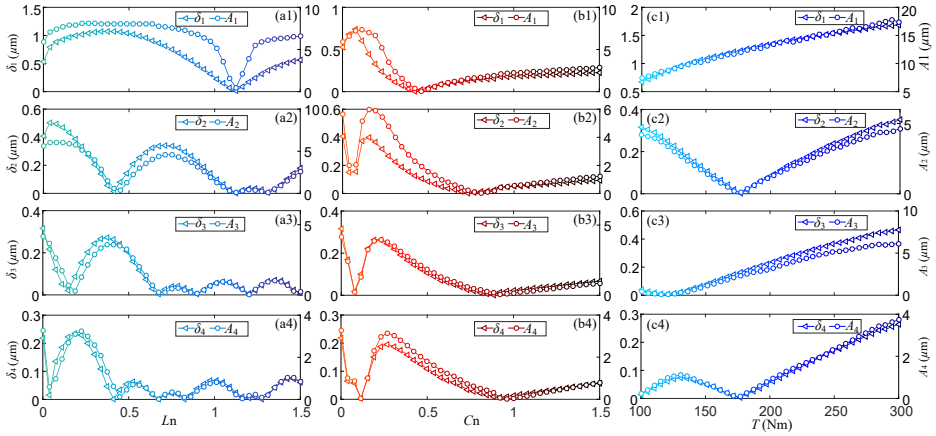


**Figure 18.** Variation trends of $\delta_{n=1,2,3,4}$ and $A_{n=1,2,3,4}$ (peak values) in terms of: (**a1–a4**) modification length $L_n$; (**b1–b4**) modification amount $C_n$; and (**c1–c4**) applied torque $T$.

### *6.2. Applications of Tip Relief Design*

Applications of tip relief design are discussed in this section. According to Section 3.1, the tip relief design depends on a double-searching process, including global search and local search. For the present study (gear pair B, linear tip relief), the length and amount of the modification $L_n, C_n \in [0, 1.5]$ are orthogonally and uniformly scattered on a map $40 \times 40$ (refer to Figure 4a).

Global searching is performed after parametric initializations. Figure 19a–e summarize contour maps of $\mathcal{L}_G$ under different applied torques, where $\mathcal{L}_G > 1$ indicates the overall fluctuation of LSTE is reduced after tip relief, and vice versa. The global search forms "L" shapes of $\mathcal{L}_G$ (warm colors in Figure 19a–e). Proper gropes of $(L_\mathrm{n}, C_\mathrm{n})$ should be located in these "L" shapes (namely the set $\mathbb{S}_G$), otherwise, improper mesh excitations would conversely make the overall LSTE fluctuations enlarged (cold colors in Figure 19a–e). The results also indicate that selections of $(L_\mathrm{n}, C_\mathrm{n})$ are sensitive to the loading condition. As the applied torque $T$ increases, the "L" shape trends move to higher values of $L_\mathrm{n}, C_\mathrm{n}$ with faded warm colors, since larger tooth deviations are required to maintain the system equilibrium. Figure 19f further outlines the boundaries of the set $\mathbb{S}_G$ by tracking isolines at $\mathcal{L}_G = 1$. It can be observed that both dimensions and locations of boundaries are significantly changed by the applied torque $T$.

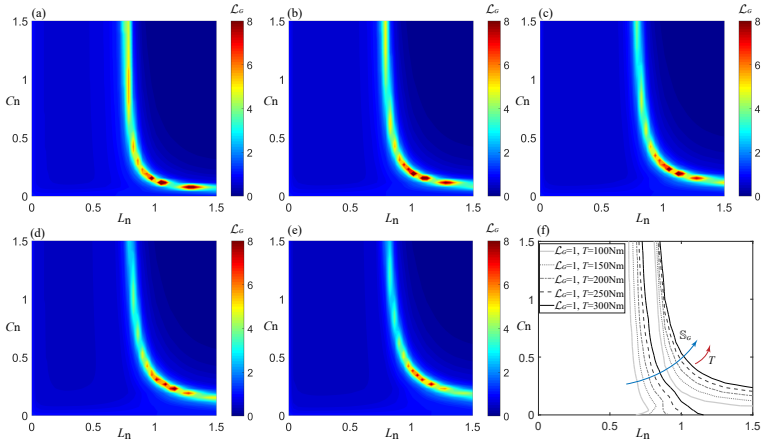


**Figure 19.** Contour maps of $\mathcal{L}_G$ for gear pair B: (**a**) $T = 100$ Nm; (**b**) $T = 150$ Nm; (**c**) $T = 200$ Nm; (**d**) $T = 250$ Nm; (**e**) $T = 300$ Nm; (**f**) Boundaries of $\mathbb{S}_G$.

Through the global searching process, the set $\mathbb{S}_G$ makes overall fluctuation amplitudes of LSTE after modification smaller than before, laying a "safe" precondition for the subsequent local searching. To emphasize the necessity of this precondition, Figure 20 displays contour maps of higher-order harmonic contents. Contour maps of $\delta_{3,4}$ (Figure 20a,b) present a fluctuated distribution in terms of $L_\mathrm{n}, C_\mathrm{n}$. Without the constraint of the global searching, some selected parameters $L_\mathrm{n}, C_\mathrm{n}$ may beyond boundaries in Figure 19f, introducing excessive spacing errors to conversely intensify vibrations.

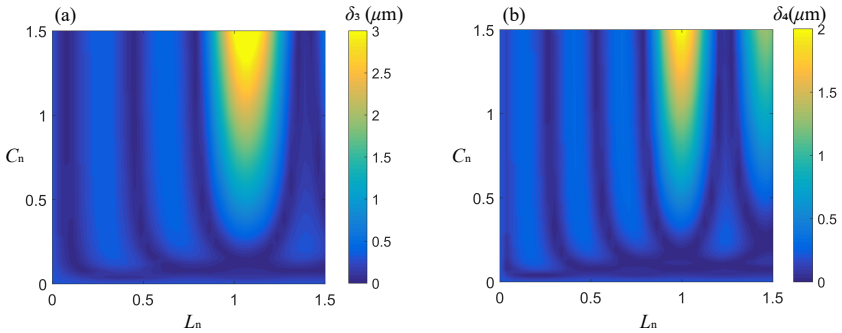


**Figure 20.** Contour maps of higher-order harmonic contents of LSTE for gear pair B ($T = 100$ Nm): (**a**) $\delta_3$; (**b**) $\delta_4$.

Next, the local search process is performed. Weigh coefficients in Equation (17) are adopted to intentionally weaken the $n^{\mathrm{th}}, n = 1, 2, 3, 4$ harmonic resonance peaks. Examples of the local search results for gear pair B ($H = 5$, $T = 100, 300$ Nm) are shown in Figure 21. The set $\mathbb{S}_L$ in the local search collects the optimized tip relief parameters, which can be

evaluated by the first $H$ maximum values of $\mathcal{L}_L$ (refer to Equations (16)–(18)). It can be observed that the boundary of $\mathbb{S}_G$ successfully constrains the local search, and the set $\mathbb{S}_L$ formed by the local search is strictly located within $\mathbb{S}_G$.

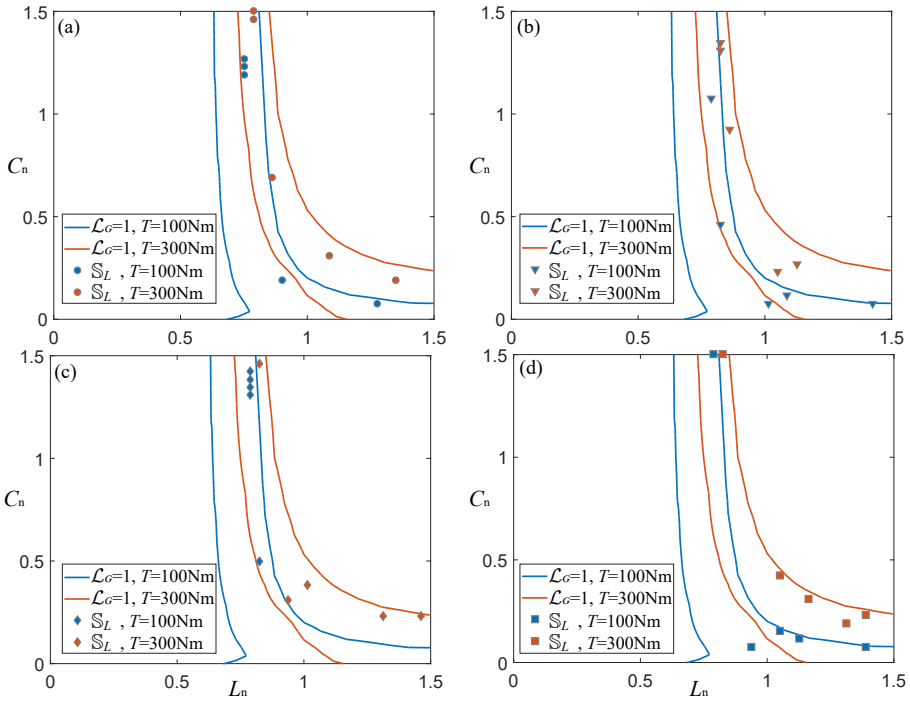


**Figure 21.** Results of the local search process with different combinations of weight coefficients: (**a**) $\mathbf{W} = \{0,1,0,0\}$; (**b**) $\mathbf{W} = \{0,1,0,0\}$; (**c**) $\mathbf{W} = \{0,0,1,0\}$; (**d**) $\mathbf{W} = \{0,0,0,1\}$.

Extracting the above results of $(L_n, C_n)$, Figure 22a shows reshaped waveforms of LSTE ($T = 100$ Nm, $\mathbf{W} = \{0,1,0,0\}$). Compared with the unmodified case, fluctuation amplitudes of reshaped waveforms are evidently reduced due to the global searching process. Different locations of $(L_n, C_n)$ in Figure 22a induce distinct combinations of harmonic contents, forming different shapes of the LSTE waveforms. In fact, these waveforms share the same function to intentionally reduce the 2$^{nd}$ order of harmonic content (i.e., $\delta_2$). In Figure 22b, each modified case presents low levels of the ratio $\delta_2(T,\wp)/\delta_2(T,\mathbf{0})$, indicating that the local search process can achieve the expected effects.

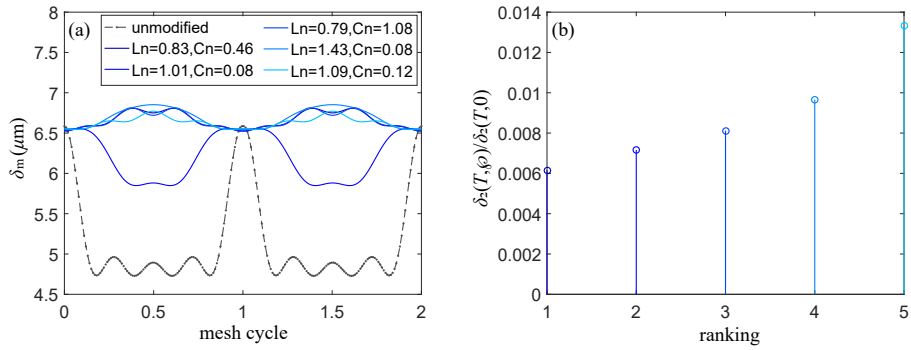


**Figure 22.** Characteristics of LSTE after the local search process ($T = 100$ Nm, $\mathbf{W} = \{0,1,0,0\}$): (**a**) 4th-order Fourier LSTE waveforms (**b**) the ratio for $\delta_2$ between the modified cases, $\delta_2(T,\wp)$, and the unmodified case, $\delta_2(T,\mathbf{0})$.

Dynamic analyses are further performed to examine the effectiveness of vibration reductions. In the condition $T = 100$ Nm, Figure 23 compares $A_{rms}$ of DTE between modified and unmodified cases. In general, compared with the unmodified case, overall magni-

tudes of $A_{\mathrm{rms}}$ are effectively reduced by each of the modified cases. Moreover, as clearly reflected in Figure 23a–d, for cases with $\mathbf{W} = \{1,0,0,0\}$, $\mathbf{W} = \{0,1,0,0\}$, $\mathbf{W} = \{0,0,1,0\}$, and $\mathbf{W} = \{0,0,0,1\}$, harmonic resonance peaks at $f_{\mathrm{m}}/f_{\mathrm{n}} = 1,\ 1/2,\ 1/3$, and $1/4$ are greatly weakened.

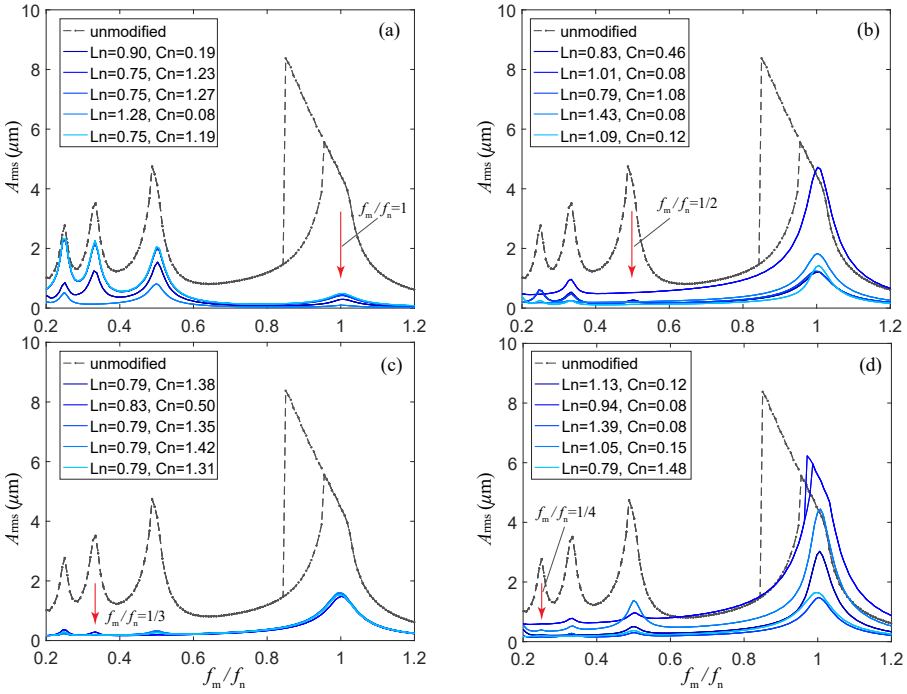


**Figure 23.** Comparisons of $A_{\mathrm{rms}}$ for gear pair B ($T = 100$ Nm, $R_{\mathrm{int}} = 22.5$ mm) at different targets of harmonic resonance reductions: (**a**) $\mathbf{W} = \{0,1,0,0\}$; (**b**) $\mathbf{W} = \{0,1,0,0\}$; (**c**) $\mathbf{W} = \{0,0,1,0\}$; (**d**) $\mathbf{W} = \{0,0,0,1\}$.

To check the robustness of the proposed method for different applied torques, $A_{\mathrm{rms}}$ of DTE between modified and unmodified cases at $T = 300$ Nm are further compared in Figure 24. Likewise, as observed in in Figure 24a–d, for cases $\mathbf{W} = \{1,0,0,0\}$, $\mathbf{W} = \{0,1,0,0\}$, $\mathbf{W} = \{0,0,1,0\}$, and $\mathbf{W} = \{0,0,0,1\}$, harmonic resonance amplitudes at $f_{\mathrm{m}}/f_{\mathrm{n}} = 1, 1/2, 1/3$, and $1/4$ are effectively reduced. Both results in Figures 23 and 24 show effective vibration reductions at different working conditions, indicating the effectiveness of the proposed method.

Figure 25 exhibits a series of steady-state solutions to further check the effectiveness in the time domain, where the case $\mathbf{W} = \{0,0,1,0\}$ with $T = 300$ Nm is selected. Figure 25a displays the phase portraits of $\tilde{q}_{\mathrm{m}} - d\tilde{q}_{\mathrm{m}}/dt$, where $\tilde{q}_{\mathrm{m}}$ represents the oscillating DTE after the mean removal. Both the oscillating DTE and the vibration velocity are significantly reduced by tip relief, resulting in much smaller orbits of the phase portraits compared with the unmodified case. Analogous results are reflected by time series in Figure 25b,c, where amplitudes of both oscillating DTE and dynamic mesh force are effectively reduced.

In summary, adaptive vibration reductions in both frequency and time domains indicate the effectiveness of the proposed tip relief design method. As a key vibration subsystem of the entire transmission system (e.g., planetary train, ordinary gear train), spur gear pairs collaboratively work with other components. Vibration signals outputted by the spur gear further serve as inputs to other components. A relatively adaptive and robust control of the vibration harmonics can effectively weaken the outputted vibration signal near adverse frequencies (e.g., resonance frequencies of other components), facilitating the collective adjustment of design parameters for the entire system.

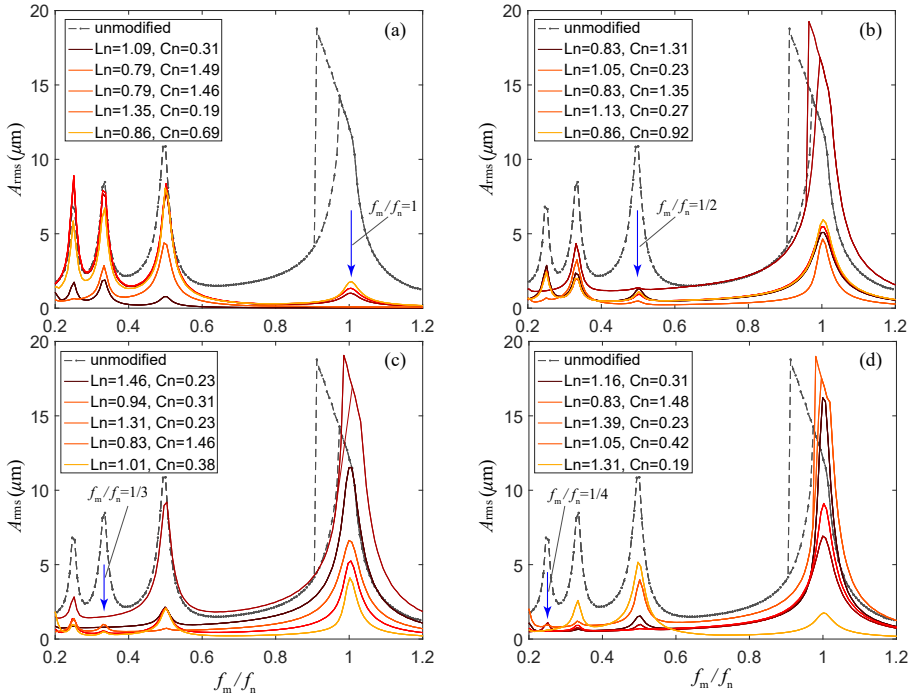


**Figure 24.** Comparisons of $A_{\text{rms}}$ for gear pair B ($T = 300$ Nm, $R_{\text{int}} = 22.5$ mm) at different targets of harmonic resonance reductions: (**a**) $\mathbf{W} = \{0,1,0,0\}$; (**b**) $\mathbf{W} = \{0,1,0,0\}$; (**c**) $\mathbf{W} = \{0,0,1,0\}$; (**d**) $\mathbf{W} = \{0,0,0,1\}$.

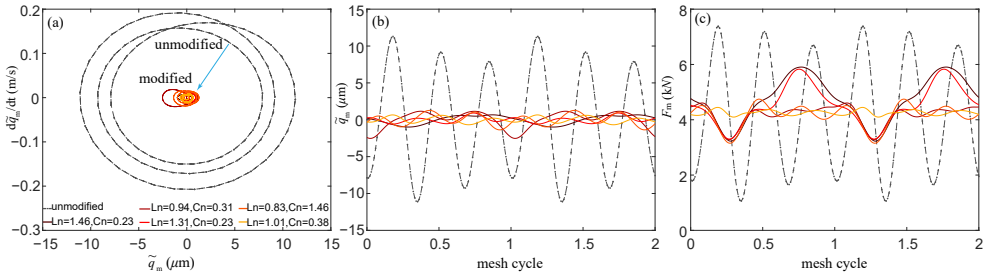


**Figure 25.** Steady-state solutions at the $f_n/3$ super-harmonic peak for modified/unmodified gear pair B ($T = 300$ Nm, $R_{\text{int}} = 22.5$ mm): (**a**) phase portraits; (**b**) oscillating DTE; (**c**) dynamic mesh force.

## 7. Conclusions

This paper proposes an analytical framework for tip relief modeling and design in spur gears, offering a fast and effective strategy to flexibly reduce vibration intensities under target working conditions. Benchmark FEMs, experimental comparisons, and application examples confirm the feasibility and effectiveness of the present framework. The findings and contributions are drawn as follows:

- Load-dependent excitation waveforms are well-captured by the proposed mesh excitation model, enabling fast evaluations of mesh excitation harmonics for tip relief design. Meanwhile, comparisons with FEMs demonstrate adaptability for various spur gear typologies, tip relief configurations, and applied torques.
- Instead of the typical peak-to-peak reduction of LSTE curves, the proposed tip relief design method decomposes mesh excitations into a Fourier series and recombines harmonic contents through a double-searching process. Application examples confirm its effectiveness in vibration reductions across different applied torques and operating speeds.
- Extensive parametric studies reveal harmonic correlations between LSTE and DTE. Interestingly, each order of harmonic content in LSTE and DTE presents consistent

variation trends and monotonicity in terms of multiple parameters, providing a key guideline for initial tip relief design.

Due to uncertainties in gear manufacturing and the complexities of gear transmission systems, the current optimization results may not be the ultimate results. Future work will focus on more detailed investigations of tip relief design with manufacturing imperfections. Nevertheless, the current analytical framework aims to broaden the scope of tip relief modeling and design for spur gear elements, which can be potentially extended for multi-stage gear systems.

**Author Contributions:** Conceptualization, original draft preparation, data curation, formal analysis, X.Z.; writing—review and editing, W.Z. and G.L.; proofreading and editing, Y.H. All authors have read and agreed to the published version of the manuscript.

**Funding:** This work is supported by the China Postdoctoral Science Foundation and the National Science Foundation (grant no. 2329791).

**Data Availability Statement:** Data are contained within the article.

**Acknowledgments:** The first author would like to express special acknowledgments to his wife for spiritual encouragement. Special thanks go out to the editors and reviewers for the constructive discussions.

**Conflicts of Interest:** The authors declare no conflicts of interest.

## Nomenclature

**Alphabet**:

| | | | |
|---|---|---|---|
| $A_n$ | oscillating DTE components | $K_n$ | harmonic contents of $K_\mathrm{m}$ |
| $A_\mathrm{rms}$ | rms of oscillating DTE components | $L$ | tooth width |
| $b_\mathrm{m}$ | half-backlash | $L_\mathrm{T}, L_\mathrm{n}$ | tip relief modification lengths |
| $c_\mathrm{m}$ | viscous damping | $m_e$ | equivalent mass |
| $C_\mathrm{T}, C_\mathrm{n}$ | tip relief modification amounts | $q_\mathrm{m}$ | dynamic transmission error |
| $e_{i,j}, e_i$ | deviations of tooth, tooth pair | $R_a$,$R_b$,$R_f$ | radius of tip, base, root circles |
| $E_\mathrm{m}$ | non-loaded static transmission error | $R_m$ | fillet radius |
| $E$ | Young's modulus | $R_h$ | root form circle radius |
| $f_\mathrm{m}$, $f_\mathrm{n}$ | mesh frequency, natural frequency | $R_\mathrm{int}$ | hub bore radius |
| $F, F_1, F_2$ | static mesh forces | $S$ | shape of tip relief modification |
| $F_\mathrm{m}$ | dynamic mesh force | $S_f$ | arc-length of junction |
| $G$ | shear modulus | $t$ | time |
| $J_\mathrm{p}, J_\mathrm{g}$ | rotary inertia of pinion, gear | $T$ | applied torque |
| $K_t$ | tooth stiffness | $u_F, u_{F1}, u_{F2}$ | moment arms |
| $K_h$ | contact stiffness | $\mathbf{W}, W_{1,2,3,4}$ | weight coefficients |
| $K_f$,$K_{f12}$,$K_{f21}$ | fillet foundation stiffness | $z_\mathrm{p}, z_\mathrm{g}$ | tooth number of pinion, gear |
| $K_\mathrm{m}$ | mesh stiffness | | |

**Greeks**:

| | | | |
|---|---|---|---|
| $\alpha_F$, $\alpha_{F1}$, $\alpha_{F2}$ | action angles of $F$, $F_1$, $F_2$ | $\kappa$ | Kolosov's constant |
| $\beta_{1,2,3,4}$ | bounds of theoretical STC and DTC | $\nu$ | Poisson's ratio |
| $\delta_{i,j}, \delta_i$ | elastic mesh deflections of tooth, tooth pair | $\tau$ | angular mesh position |
| $\delta_\mathrm{m}$ | loaded static transmission error | $\varphi_{1,2}$ | bounds of simultaneous tooth contact |
| $\delta_n$ | harmonic contents of $\delta_\mathrm{m}$ | $\Phi(\tau)$ | angular tooth separation function |
| $\zeta$ | damping ratio | $\phi_K, \phi_\delta, \phi_E$ | phase angles |
| $\theta_b, \theta_f$ | half-tooth angles at base, root circles | $\Lambda_a, \Lambda_b, \Lambda_s, \Omega$ | coefficients of $K_t$ |
| $\theta_\mathrm{p}, \theta_\mathrm{g}$ | angular positions of pinion, gear | $\Psi, \Theta^{1,2}, \Theta^{2,1}$ | coefficients of $K_f$,$K_{f12}$,$K_{f21}$ |

**Subscripts**:

| | | | |
|---|---|---|---|
| $i = 1, 2$ | quantities of tooth pair 1, 2 | $n$ | harmonic orders |

**Subscripts**:

| | | | |
|---|---|---|---|
| $j = \mathrm{p}, \mathrm{g}$ | quantities of pinion, gear | $k, s$ | generic counting numbers |
| $r = \mathrm{I}, \mathrm{II}$ | quantities of tooth region I, II | | |

**Symbols:**

| | | | |
|---|---|---|---|
| $\wp$ | tip relief configurations $\{L_\mathrm{n}, C_\mathrm{n}, S\}$ | $\mathcal{L}_G$ | objective in global searching |
| inv | involute function | $\mathcal{L}_L$ | objective in local searching |
| $\mathbb{D}$ | integration intervals of $K_t$ | $\mathbb{S}_G$ | satisfied sets in global searching |
| $\mathscr{N}$ | piecewise function of backlash | $\mathbb{S}_L$ | satisfied sets in local searching |

**Abbreviations**:

| | | | |
|---|---|---|---|
| DTC | double tooth contact | LSTE | loaded static transmission error |
| ETC | extended tooth contact | NSTE | non-loaded static transmission error |
| STC | single-tooth contact | DTE | dynamic transmission error |
| LOA | line of action | FEM | finite element method |

## Appendix A. Evaluations of Tooth Stiffness Parameters

Tooth stiffness integrands $\Lambda_{a,r}$, $\Lambda_{b,r}$, $\Lambda_{s,r}$, and $\Omega_r$ in Equation (34) are as follows:

$$\Omega_r(\alpha_r) = \begin{cases} (1+\lambda_m)\sin\theta_f - \lambda_m\left(\theta_f + \alpha_r\right), & r = \mathrm{I} \\ \sin\alpha_r + (\theta_b - \alpha_r)\cos\alpha_r, & r = \mathrm{II} \end{cases} \tag{A1}$$

$$\Lambda_{a,i}(\alpha_r) = \begin{cases} \lambda_m \sin\left(\theta_f + \alpha_r\right), & r = \mathrm{I} \\ (\theta_b - \alpha_r)\cos\alpha_r, & r = \mathrm{II} \end{cases} \tag{A2}$$

$$\Lambda_{b,i}(\alpha_F, \alpha_r) = \begin{cases} 3\lambda_m\left[\lambda_b \sec\alpha_F - (1+\lambda_m)\cos\theta_f + \lambda_m\cos\left(\theta_f + \alpha_r\right)\right]^2 \sin\left(\theta_f + \alpha_r\right), & r = \mathrm{I} \\ 3[\sec\alpha_F + (\theta_b - \alpha_r)\sin\alpha_r - \cos\alpha_r]^2(\theta_b - \alpha_r)\cos\alpha_r, & r = \mathrm{II} \end{cases} \tag{A3}$$

$$\Lambda_{s,i}(\alpha_r) = \begin{cases} 1.2\lambda_m \sin\left(\theta_f + \alpha_r\right), & r = \mathrm{I} \\ 1.2(\theta_b - \alpha_r)\cos\alpha_r, & r = \mathrm{II} \end{cases}, \tag{A4}$$

where tooth dimensions are normalized by $\lambda_m = R_m/R_f$ and $\lambda_b = R_b/R_f$ for conciseness. Again, $r = \mathrm{I}$ and $r = \mathrm{II}$ separately represent the transition and involute tooth region. Integration bounds $\mathbb{D}_r$ ($r = \mathrm{I}, \mathrm{II}$) in Equation (34) are as follows:

$$\mathbb{D}_r = \begin{cases} x \in [0, d_1],\ \alpha_r \in [0, \varphi_h], & r = \mathrm{I} \\ x \in [d_1, d_2],\ \alpha_r \in [-\alpha_F, \theta_h - \alpha_h], & r = \mathrm{II} \end{cases}. \tag{A5}$$

According to the tooth geometry in Figure 6, expressions of $\varphi_h$ and $\theta_h$ hold:

$$\varphi_h = \arccos\left[\frac{(1+\lambda_m)^2 + 1 - \lambda_h^2}{2\lambda_m(1+\lambda_m)}\right],\ \theta_h = \frac{\pi}{2z} + \mathrm{inv}(\alpha_\mathrm{n}) - \mathrm{inv}(\alpha_h), \tag{A6}$$

where $\alpha_h = \arccos(R_b/R_h)$ and $\lambda_h = R_h/R_f$.

## Appendix B. Properties of Specimens

**Table A1.** Geometrical and material properties of standard spur gear pair A and B.

| Properties | Gear Pair A | | Gear Pair B | |
|---|---|---|---|---|
| | **Gear** | **Pinion** | **Gear** | **Pinion** |
| Tooth number $z$ | 30 | 30 | 50 | 50 |
| Modules $m$ (mm) | 2 | 2 | 3 | 3 |
| Tooth width $L$ (mm) | 20 | 20 | 20 | 20 |
| Pressure angle $\alpha_n$ (°) | 20 | 20 | 20 | 20 |
| Young's modulus (Gpa) | 206.8 | 206.8 | 206.8 | 206.8 |
| Poisson's ratio | 0.3 | 0.3 | 0.3 | 0.3 |
| Density (kg/m$^3$) | 7850 | 7850 | 7850 | 7850 |
| Root form circle radius $R_h$ (mm) | 28.53 | | 72.47 | |
| Fillet radius $R_m$ (mm) | 0.76 | | 1.14 | |
| Hub bore radius $R_{int}$ (mm) | 6.3 | | 22.5, 30 | |
| tip clearance coefficient | 0.25 | | 0.25 | |
| addendum coefficient | 1.00 | | 1.00 | |
| Involute contact ratio | 1.65 | | 1.75 | |
| Applied torque (Nm) | 5–200 | | 100–300 | |
| Rotational speed (rpm) | - | | 600–4100 | |
| Damping radio | - | | 0.04 | |

## Appendix C. Configuration of the Benchmark FEM Model

Figure A1 depicts the configuration of the benchmark FEM model. Based on the simulation platform Abaqus®, 4-node bilinear plane stress elements (CPS4R) are used to capture the thin-walled feature of spur gear pair B. The geometry discretization strategy is built based on the previous work [18]. Three tooth pairs (tooth pairs 1, 2, and 3) with dense FE elements are interesting analysis regions. For computational accuracy and convergence, contact elements near tooth flanks are further refined with an average size of 0.05 mm. The 2D surface-to-surface contact algorithm is used throughout contact computation. Nodes at the hub bores of the pinion and gear are constrained to their respective centers, $O_p$ and $O_g$, through rigid coupling. Steady torque and uniform rotational displacements are applied separately to the centers $O_p$ and $O_g$, in each load step.

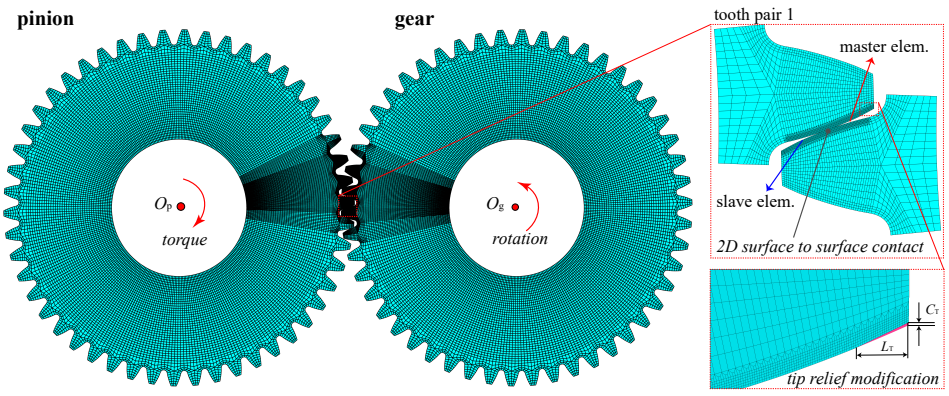


**Figure A1.** Configuration of the benchmark FEM model of gear pair B.

Unlike standard involute spur gears, the tip relief induces rigid body motions (i.e., NSTE) during the simulation. For each study case, two conditions are simulated, namely, the elastic condition and the rigid condition (approximated by 1000$E$). The elastic condition comprehensively covers mesh deformations and NSTE, while the rigid condition functions to independently evaluate NSTE. By extracting the rotational displacement in each load step, NSTE, LSTE, and mesh stiffness can be further calculated as follows:

$$E_{\mathrm{m,FEM}} = |\theta_{\mathrm{p,R}} + \theta_{\mathrm{g,R}}|R_{\mathrm{b,p}},\ \delta_{\mathrm{m,FEM}} = |\theta_{\mathrm{p,E}} + \theta_{\mathrm{g,E}}|R_{\mathrm{b,p}},$$
$$K_{\mathrm{m,FEM}} = \frac{T}{(|\theta_{\mathrm{p,E}} + \theta_{\mathrm{g,E}}| - |\theta_{\mathrm{p,R}} + \theta_{\mathrm{g,R}}|)R_{\mathrm{b,p}}^2}, \tag{A7}$$

where $E_{\mathrm{m,FEM}}$, $\delta_{\mathrm{m,FEM}}$, and $K_{\mathrm{m,FEM}}$ are NSTE, LSTE, and mesh stiffness evaluated by FEM. $\theta_{\mathrm{p,R}}$, $\theta_{\mathrm{g,R}}$ and $\theta_{\mathrm{p,E}}$, $\theta_{\mathrm{g,E}}$ are the rotational displacements extracted from the rigid and elastic conditions, respectively.

## References


1. Wang, J.; Li, R.; Peng, X. Survey of nonlinear vibration of gear transmission systems. *Appl. Mech. Rev.* **2003**, *56*, 309–329. [CrossRef]
2. Khabou, M.; Bouchaala, N.; Chaari, F.; Fakhfakh, T.; Haddar, M. Study of a spur gear dynamic behavior in transient regime. *Mech. Syst. Signal Process.* **2011**, *25*, 3089–3101. [CrossRef]
3. Li, G.; Wang, Z.; Zhu, W. A function-oriented active form-grinding method for cylindrical gears based on error sensitivity. *Int. J. Adv. Manuf. Technol.* **2017**, *92*, 3019–3031. [CrossRef]
4. Liang, X.; Zuo, M.J.; Feng, Z. Dynamic modeling of gearbox faults: A review. *Mech. Syst. Signal Process.* **2018**, *98*, 852–876. [CrossRef]
5. Chen, Z.; Zhou, Z.; Zhai, W.; Wang, K. Improved analytical calculation model of spur gear mesh excitations with tooth profile deviations. *Mech. Mach. Theory* **2020**, *149*, 103838. [CrossRef]
6. Pleguezuelos, M.; Sánchez, M.B.; Pedrero, J.I. Control of transmission error of high contact ratio spur gears with symmetric profile modifications. *Mech. Mach. Theory* **2020**, *149*, 103839. [CrossRef]
7. Pedrero, J.I.; Pleguezuelos, M.; Sánchez, M.B. Analytical model for meshing stiffness, load sharing, and transmission error for helical gears with profile modification. *Mech. Mach. Theory* **2023**, *185*, 105340. [CrossRef]
8. Chen, Z.; Ning, J.; Wang, K.; Zhai, W. An improved dynamic model of spur gear transmission considering coupling effect between gear neighboring teeth. *Nonlinear Dyn.* **2021**, *106*, 339–357. [CrossRef]
9. Alam, J.; Panda, S.; Dash, P. A comprehensive review on design and analysis of spur gears. *Int. J. Interact. Des. Manuf.* **2023**, *17*, 993–1019. [CrossRef]
10. Harris, S.L. Dynamic loads on the teeth of spur gears. *Proc. Inst. Mech. Eng.* **1958**, *172*, 87–112. [CrossRef]
11. Natali, C.; Battarra, M.; Dalpiaz, G.; Mucchi, E. A critical review on Fe-based methods for mesh stiffness estimation in spur gears. *Mech. Mach. Theory* **2021**, *161*, 104319. [CrossRef]
12. Marafona, J.D.; Marques, P.M.; Martins, R.C.; Seabra, J.H. Mesh stiffness models for cylindrical gears: A detailed review. *Mech. Mach. Theory* **2021**, *166*, 104472. [CrossRef]
13. Miler, D.; Hoic, M. Optimisation of cylindrical gear pairs: A review. *Mech. Mach. Theory* **2021**, *156*, 104156. [CrossRef]
14. Wang, J.; Howard, I. Finite Element Analysis of High Contact Ratio Spur Gears in Mesh. *J. Tribol.* **2005**, *127*, 469–483. [CrossRef]
15. Pedersen, N.L.; Jørgensen, M.F. On gear tooth stiffness evaluation. *Comput. Struct.* **2014**, *135*, 109–117. [CrossRef]
16. He, Z.; Hu, Y.; Zheng, X.; Yu, Y. A calculation method for tooth wear depth based on the finite element method that considers the dynamic mesh force. *Machines* **2022**, *10*, 69. [CrossRef]
17. Ma, H.; Yang, J.; Song, R.; Zhang, S.; Wen, B. Effects of tip relief on vibration responses of a geared rotor system. *Proc. Inst. Mech. Eng. Part C J. Mech. Eng. Sci.* **2014**, *228*, 1132–1154. [CrossRef]
18. Zheng, X.; Luo, W.; Hu, Y.; He, Z.; Wang, S. Study on the mesh stiffness and nonlinear dynamics accounting for centrifugal effect of high-speed spur gears. *Mech. Mach. Theory* **2022**, *170*, 104686. [CrossRef]
19. Zhan, J.; Fard, M.; Jazar, R. A CAD-FEM-QSA integration technique for determining the time-varying meshing stiffness of gear pairs. *Measurement* **2017**, *100*, 139–149. [CrossRef]
20. Liang, X.; Zhang, H.; Zuo, M.J.; Qin, Y. Three new models for evaluation of standard involute spur gear mesh stiffness. *Mech. Syst. Signal Process.* **2018**, *101*, 424–434. [CrossRef]
21. Benaïcha, Y.; Perret-Liaudet, J.; Beley, J.-D.; Rigaud, E.; Thouverez, F. On a flexible multibody modelling approach using FE-based contact formulation for describing gear transmission error. *Mech. Mach. Theory* **2022**, *167*, 104505. [CrossRef]
22. Parker, R.; Vijayakar, S.; Imajo, T. Non-linear dynamic response of a spur gear pair: Modelling and experimental comparisons. *J. Sound Vib.* **2000**, *237*, 435–455. [CrossRef]
23. Cooley, C.G.; Liu, C.; Dai, X.; Parker, R.G. Gear tooth mesh stiffness: A comparison of calculation approaches. *Mech. Mach. Theory* **2016**, *105*, 540–553. [CrossRef]
24. Wagaj, P.; Kahraman, A. Influence of tooth profile modification on helical gear durability. *J. Mech. Des.* **2002**, *124*, 501–510. [CrossRef]
25. Vedmar, L.; Henriksson, B. A general approach for determining dynamic forces in spur gears. *J. Mech. Des.* **1998**, *120*, 593–598. [CrossRef]

26. Fernández del Rincón, A.; Viadero, F.; Iglesias, M.; García, P.; de Juan, A.; Sancibrián, R. A model for the study of meshing stiffness in spur gear transmissions. *Mech. Mach. Theory* **2013**, *61*, 30–58. [CrossRef]
27. Xie, C.; Hua, L.; Lan, J.; Han, X.; Wan, X.; Xiong, X. Improved analytical models for mesh stiffness and load sharing ratio of spur gears considering structure coupling effect. *Mech. Syst. Signal Process.* **2018**, *111*, 331–347. [CrossRef]
28. Chen, K.; Huangfu, Y.; Ma, H.; Xu, Z.; Li, X.; Wen, B. Calculation of mesh stiffness of spur gears considering complex foundation types and crack propagation paths. *Mech. Syst. Signal Process.* **2019**, *130*, 273–292. [CrossRef]
29. Pedrero, J.I. Analytical model for spur gears with profile modification: Simulation of the meshing stiffness, load sharing, and transmission error. In *Machine and Industrial Design in Mechanical Engineering*; Rackov, M., Mitrovic, R., Čavić, M., Eds.; Springer International Publishing: Cham, Switzerland, 2022; pp. 3–26. [CrossRef]
30. Weber, C. *The Deformation of Loaded Gears and the Effect on Their Load-Carrying Capacity, Sponsored Research (Germany)*; Department of Scientific and Industrial Research: London, UK, 1951; Report 3.
31. Yang, D.C.H.; Lin, J.Y. Hertzian damping, tooth friction and bending elasticity in gear impact dynamics. *J. Mech. Des. Trans. ASME* **1987**, *109*, 189–196. [CrossRef]
32. Tian, X. Dynamic Simulation for System Response of Gearbox Including Localized Gear Faults. Master's Thesis, University of Alberta, Edmonton, AB, Canada, 2004.
33. Sainsot, P.; Velex, P.; Duverger, O. Contribution of gear body to tooth deflections—A new bidimensional analytical formula. *J. Mech. Des.* **2004**, *126*, 748–752. [CrossRef]
34. Xie, C.; Hua, L.; Han, X.; Lan, J.; Wan, X.; Xiong, X. Analytical formulas for gear body-induced tooth deflections of spur gears considering structure coupling effect. *Int. J. Mech. Sci.* **2018**, *148*, 174–190. [CrossRef]
35. Velex, P.; Bruyère, J.; Houser, D.R. Some analytical results on transmission errors in narrow-faced spur and helical gears: Influence of profile modifications. *J. Mech. Des.* **2011**, *133*, 031010. [CrossRef]
36. Chen, Z.; Shao, Y. Mesh stiffness calculation of a spur gear pair with tooth profile modification and tooth root crack. *Mech. Mach. Theory* **2013**, *62*, 63–74. [CrossRef]
37. Sánchez, M.B.; Pleguezuelos, M.; Pedrero, J.I. Influence of profile modifications on meshing stiffness, load sharing, and transmission error of involute spur gears. *Mech. Mach. Theory* **2019**, *139*, 506–525. [CrossRef]
38. Sánchez, M.B.; Pleguezuelos, M.; Pedrero, J.I. Influence of profile modification on the transmission error of spur gears under surface wear. *Mech. Mach. Theory* **2024**, *191*, 105473. [CrossRef]
39. Ghosh, S.; Chakraborty, G. On optimal tooth profile modification for reduction of vibration and noise in spur gear pairs. *Mech. Mach. Theory* **2016**, *105*, 145–163. [CrossRef]
40. Ma, H.; Pang, X.; Feng, R.; Wen, B. Evaluation of optimum profile modification curves of profile shifted spur gears based on vibration responses. *Mech. Syst. Signal Process.* **2016**, *70–71*, 1131–1149. [CrossRef]
41. Cirelli, M.; Giannini, O.; Valentini, P.P.; Pennestrì, E. Influence of tip relief in spur gears dynamic using multibody models with movable teeth. *Mech. Mach. Theory* **2020**, *152*, 103948. [CrossRef]
42. Palmer, D.; Fish, M. Evaluation of Methods for Calculating Effects of Tip Relief on Transmission Error, Noise and Stress in Loaded Spur Gears. *Gear Technol.* **2012**, *29*, 56–67. Available online: https://www.geartechnology.com/ext/resources/issues/0112x/palmer.pdf?1633055047 (accessed on 16 February 2025).
43. Hajjaj, A.; Corrigan, K.; Mohammadpour, M.; Theodossiades, S. On the stability analysis of gear pairs with tooth profile modification. *Mech. Mach. Theory* **2022**, *174*, 104888. [CrossRef]
44. Magalhães, L.; Martins, R.; Locateli, C.; Seabra, J. Influence of tooth profile and oil formulation on gear power loss. *Tribol. Int.* **2010**, *43*, 1861–1871. [CrossRef]
45. Kimiaei, M.; Akbarzadeh, S. Effect of profile modification on the performance of spur gears in isothermal mixed-EHL regime using load-sharing concept. *Proc. Inst. Mech. Eng. Part J J. Eng. Tribol.* **2019**, *233*, 936–948. [CrossRef]
46. Li, S.; Anisetti, A. A tribo-dynamic contact fatigue model for spur gear pairs. *Int. J. Fatigue* **2017**, *98*, 81–91. [CrossRef]
47. Ouyang, T.; Huang, H.; Zhou, X.; Pan, M.; Chen, N.; Lv, D. A finite line contact tribo-dynamic model of a spur gear pair. *Tribol. Int.* **2018**, *119*, 753–765. [CrossRef]
48. Wen, Q.; Du, Q.; Zhai, X. An analytical method for calculating the tooth surface contact stress of spur gears with tip relief. *Int. J. Mech. Sci.* **2019**, *151*, 170–180. [CrossRef]
49. Elisaus, V.; Mohammadpour, M.; Theodossiades, S.; Rahnejat, H. Effect of teeth micro-geometrical form modification on contact kinematics and efficiency of high performance transmissions. *Proc. Inst. Mech. Eng. Part K J. Multibody Dyn.* **2017**, *231*, 538–555. [CrossRef]
50. Cazan, S.; Dănilă, C.; Cretu, S. Tooth contact analysis of helical gears using semi-analytical methods in real gearing situations. *Tribol. Int.* **2023**, *185*, 108482. [CrossRef]
51. Chen, Z.; Zhang, J.; Zhai, W.; Wang, Y.; Liu, J. Improved analytical methods for calculation of gear tooth fillet-foundation stiffness with tooth root crack. *Eng. Fail. Anal.* **2017**, *82*, 72–81. [CrossRef]

52. Chen, Z.; Zhai, W.; Wang, K. Vibration feature evolution of locomotive with tooth root crack propagation of gear transmission system. *Mech. Syst. Signal Process.* **2019**, *115*, 29–44. [CrossRef]
53. Bahk, C.-J.; Parker, R.G. Analytical investigation of tooth profile modification effects on planetary gear dynamics. *Mech. Mach. Theory* **2013**, *70*, 298–319. [CrossRef]
54. Öztürk, V.Y.; Cigeroglu, E.; Özguven, H.N. Ideal tooth profile modifications for improving nonlinear dynamic response of planetary gear trains. *J. Sound Vib.* **2021**, *500*, 116007. [CrossRef]
55. Ma, H.; Pang, X.; Feng, R.; Song, R.; Wen, B. Fault features analysis of cracked gear considering the effects of the extended tooth contact. *Eng. Fail. Anal.* **2015**, *48*, 105–120. [CrossRef]
56. Ma, H.; Zeng, J.; Feng, R.; Pang, X.; Wen, B. An improved analytical method for mesh stiffness calculation of spur gears with tip relief. *Mech. Mach. Theory* **2016**, *98*, 64–80. [CrossRef]
57. Sun, Y.; Ma, H.; Huangfu, Y.; Chen, K.; Che, L.; Wen, B. A revised time-varying mesh stiffness model of spur gear pairs with tooth modifications. *Mech. Mach. Theory* **2018**, *129*, 261–278. [CrossRef]
58. Li, Z.; Chen, Z.; Zhai, W. Nonlinear dynamic characteristics of a spur gear pair considering extended tooth contact and coupling effect between gear neighboring teeth. *Nonlinear Dyn.* **2023**, *111*, 2395–2414. [CrossRef]
59. Zheng, X.; Hu, Y.; He, Z.; Xiao, Y.; Zhang, X. On the extended tooth contact and nonlinear dynamics for spur gears—An analytical model. *Mech. Mach. Theory* **2022**, *175*, 104958. [CrossRef]
60. Zheng, X.; Luo, W.; Hu, Y.; He, Z.; Wang, S. Analytical approach to mesh stiffness modeling of high-speed spur gears. *Int. J. Mech. Sci.* **2022**, *224*, 107318. [CrossRef]
61. Velex, P.; Ajmi, M. Dynamic tooth loads and quasi-static transmission errors in helical gears—Approximate dynamic factor formulae. *Mech. Mach. Theory* **2007**, *42*, 1512–1526. [CrossRef]
62. Liu, C.; Shi, W.; Curá, F.M.; Mura, A. A novel method to predict static transmission error for spur gear pair based on accuracy grade. *J. Cent. South Univ.* **2020**, *27*, 3334–3349. [CrossRef]
63. Li, H.; Chen, S.; Tang, J.; Chen, W.; Ouyang, H. A novel approach for calculating no-load static transmission error based on measured discrete tooth surfaces. *Mech. Mach. Theory* **2019**, *138*, 112–123. [CrossRef]
64. Kahraman, A.; Blankenship, G.W. Effect of involute tip relief on dynamic response of spur gear pairs. *J. Mech. Des.* **1999**, *121*, 313–315. [CrossRef]
65. Xie, C.; Shu, X. A new mesh stiffness model for modified spur gears with coupling tooth and body flexibility effects. *Appl. Math. Model.* **2021**, *91*, 1194–1210. [CrossRef]
66. *BS 1970:2012*; Spur and Helical Gears—Basic Rack Form, Modules and Accuracy. BSI Standards: London, UK, 2012.
67. *ISO 1122-1:1983*; Glossary of Gear Terms-Part 1: Geometrical Definitions. International Organization for Standardization (ISO): Geneva, Switzerland, 1983.
68. Özguven, H.N.; Houser, D. Mathematical models used in gear dynamics—A review. *J. Sound Vib.* **1988**, *121*, 383–411. [CrossRef]
69. Wan, Z.; Cao, H.; Zi, Y.; He, W.; He, Z. An improved time-varying mesh stiffness algorithm and dynamic modeling of gear-rotor system with tooth root crack. *Eng. Fail. Anal.* **2014**, *42*, 157–177. [CrossRef]
70. Cui, L.; Zhai, H.; Zhang, F. Research on the meshing stiffness and vibration response of cracked gears based on the universal equation of gear profile. *Mech. Mach. Theory* **2015**, *94*, 80–95. [CrossRef]
71. Liang, X.; Zhang, H.; Liu, L.; Zuo, M.J. The influence of tooth pitting on the mesh stiffness of a pair of external spur gears. *Mech. Mach. Theory* **2016**, *106*, 1–15. [CrossRef]
72. Palmgren, A. *Ball and Roller Bearing Engineering*; SKF Industries Inc.: Philadelphia, PA, USA, 1945.
73. Cornell, R.W. Compliance and stress sensitivity of spur gear teeth. *J. Mech. Des.* **1981**, *103*, 447–459. [CrossRef]
74. Tse, D.; Lin, H. Separation distance and static transmission error of involute spur gears. In Proceedings of the 28th Joint Propulsion Conference and Exhibit, Nashville, TN, USA, 6–8 July 1992; p. 3490.


**Disclaimer/Publisher's Note:** The statements, opinions and data contained in all publications are solely those of the individual author(s) and contributor(s) and not of MDPI and/or the editor(s). MDPI and/or the editor(s) disclaim responsibility for any injury to people or property resulting from any ideas, methods, instructions or products referred to in the content.